Nano Today 16 (2017) 30–45

Contents lists available at ScienceDirect

Nano Today

journal homepage: www.elsevier.com/locate/nanotoday

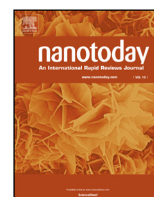

Review

Engineering two-dimensional electronics by semiconductor defects

Dan Wang [a], Xian-Bin Li [a,*], Dong Han [b], Wei Quan Tian [c], Hong-Bo Sun [a,*]

[a] State Key Laboratory on Integrated Optoelectronics, College of Electronic Science and Engineering, Jilin University, Changchun 130012, China
[b] State Key Laboratory of Luminescence and Applications, Changchun Institute of Optics, Fine Mechanics and Physics, Chinese Academy of Sciences, Changchun 130033, China
[c] College of Chemistry and Chemical Engineering, Chongqing University, Huxi Campus, Chongqing 401331, China

ARTICLE INFO

Article history:
Received 19 May 2017
Received in revised form 4 July 2017
Accepted 6 July 2017
Available online 25 September 2017

ABSTRACT

Two-dimensional (2D) semiconductors have attracted considerable attentions from electronic-engineering community due to their unique electronic properties. Especially, the inherent advantage of scaling semiconductor into atomic thickness has raised the prospect of possible extension of the Moore's law. To achieve 2D electronics, a full comprehension of semiconductor defect physics and chemistry is indispensable due to its decisive role in controlling electrical performance of 2D materials and functionalizing their devices. In this review, first we explain why 2D semiconductors is important for nanoelectronics and optoelectronics. Second, we elucidate how native defects or intentional impurities affect and control electrical characteristic in 2D semiconductors, such as carrier concentration and their conductive type. In this section, experimental pictures of defects and several updated theoretical methods to evaluate ionization energies of defects and their conductive type are introduced in detail. Third, typical device experiments are shown to demonstrate a direct role of defects to functionalize 2D electronic device. Furthermore, a database of popular defects and their electrical properties in current popular 2D semiconductors is summarized for references. Last, we discuss the challenges and potential prospects of defect engineering for 2D devices. The present paper offers important viewpoints from semiconductor defects to design the emerging 2D electronics.

© 2017 Elsevier Ltd. All rights reserved.

Contents

Introduction 30
Experimental characterization of defect 32
Atomic resolution imaging 32
Raman and photoluminescence spectroscopy 34
Theoretical evaluation on carrier ionization energy of defect for conductivity 35
Ionization energy (evaluated by ground-state electronic structure) 35
The difference between single-particle levels and transition levels 37
Ionization energy (evaluated by transition level) 37
Roles of defect in engineering 2D electronic devices 40
Realization of *n*/*p*-type conductivity for devices by defect 40
Device performances associated with defects 41
Conclusion and prospect 44
Acknowledgements 44
References 44

Introduction

Two-dimensional (2D) materials are substances with atomic thickness in which electrons are allowed to move freely in 2D plane but restricted in out-of-plane direction [1–3]. Dimensionality reduction brings 2D materials quantum confinement and weak

* Corresponding authors.
E-mail addresses: lixianbin@jlu.edu.cn (X.-B. Li), hbsun@jlu.edu.cn (H.-B. Sun).

http://dx.doi.org/10.1016/j.nantod.2017.07.001
1748-0132/© 2017 Elsevier Ltd. All rights reserved.

dielectric screening which in turn endow them unique properties [4–6]. The era of 2D materials begins with the successful isolation of graphene [7]. While it shows great potential in many advanced technological fields, especially in electronics due to its ultrahigh electron mobility [8,9], the lack of bandgap limits its application in high-performance filed effect transistors (FETs) [8–10]. To address this, researchers make great efforts to open a sizeable gap of graphene [11–17]. At the same time, mining 2D semiconducting counterparts has also sparked the community's interests. Following graphene, more than ten different layered semiconductors including silicene [18], germanene [19], stanene [20,21], black phosphorus (BP) [22–24], group-III monochalcogenides [25], transition metal dichalcogenides (TMDs) [26–29], and hexagonal boron nitride (BN) [3,30,31] have been successfully prepared by experiments. Their bandgaps range from a few millielectronvolts to several electronvolts. Moreover, the band structures depend on the number of layers [32], such as a transition from indirect gap in the bulk MoS_2 (1.2 eV) to direct gap in monolayer MoS_2 (1.8–2.8 eV) [28,33]. In addition, these materials can be stacked layer by layer in desired sequence to create new functional counterparts. Furthermore, the ultrathin nature of 2D semiconductors which allows high integration density has motivated the research in 2D electronic devices.

Following the Moore's law, the dimensions of FETs continue to decrease [2]. However, FETs cannot be scaled down infinitely. The scaling limitation of Si FETs is predicted to be 5 nanometers under which severe short channel effects (SCE) occur [2,34]. SCE refers to the difficulty of heat dissipation caused by increased static power, which is associated with increased source-to-drain leakage current [35,36]. Plentiful researches has been devoted to explore new channel materials which can mitigate SCE and then extend the Moore's law. In fact, 2D semiconductors are considered as one of the most promising candidates due to their excellent gate electrostatics and the reduced SCE, which could result in lower power consumption and high-level device integration [2]. For FETs, the mobile charges distribute widely in three-dimensional (3D) materials (Fig. 1(a)) whereas in 2D materials the charged carriers are confined in the atomically thin 2D channel with a narrow distribution (Fig. 1(b)). Hence, the carriers are more easily and uniformly controlled via gate voltage in 2D materials [37]. On the other hand, Reducing thickness of 3D materials will enhance gate electrostatic but degrade its FET performance [38]. The degradation comes from the carrier scattering and interface trap states caused by the undesirable dangling bonds in the surfaces of 3D materials (see left of Fig. 1(a)). In contrast, 2D materials are free of dangling bonds (see left of Fig. 1(b)). In fact, MoS_2 has been theoretically predicted to be superior to Si [27,39,40]. With the Wentzel-Kramers-Brillouin approximation, Desai et al. [27] calculated the source-to-drain tunneling currents in the OFF state for different channel thickness and gate lengths of Si and MoS_2, as shown in Fig. 1(c) and (d). For the same gate length (Fig. 1(c)), in MoS_2, the source-to-drain currents in OFF state are two order of magnitude smaller than that in silicon. For similar channel thickness (Fig. 1(d)), MoS_2 transistor can be scaled to shorter gate length than Si. These results reveal the potential advantages of 2D semiconductors as next-generation channel materials for high-performance devices. More encouragingly, a 1-nm-gate-length FET using single-walled carbon nanotube as gate and bilayer MoS_2 as channel has been demonstrated at the end of 2016 [27], as shown in Fig. 1(e). It exhibits near ideal switching characteristics with an on-off current ratio of 10^6 and a subthreshold swing of 65 mV/dec, see Fig. 1(f). Also, a complementary metal oxide semiconductor (CMOS) technology made from *n*-type and *p*-type WSe_2 FETs has been demonstrated [41]. Furthermore, in 2017 Wachter et al. [42] presented a microprocessor consisting of 115 MoS_2 transistors, see Fig. 1(g). The device shows good operability and then demonstrates the feasibility of using 2D semiconductors to realize complex digital circuit.

In addition to the nanoelectronic devices above, 2D semiconductors also have a potential in optoelectronics [43,44]. *p-n* junctions, which are the basic building blocks of traditional 3D-semiconductor optoelectronic devices including photodetector, light-emitting diode, and solar cell, have been demonstrated in 2D materials. For example, Pospischil et al. [45] reported a lateral *p-n* junction based on electrostatically doped WSe_2, as shown in Fig. 2(a). Two splitting gate electrodes are coupled to two different regions of a WSe_2 flake. Biasing one gate with a positive voltage and the other with a negative voltage draws electrons and holes into the channel respectively, and thus a *p-n* junction is realized. Under optical illumination, the junctions show photo-voltaic response, see the green solid line in Fig. 2(b). Also, Lee et al. [46] realized a vertical *p-n* junction consisting of monolayer MoS_2 (*n*-type) and WSe_2 (*p*-type) as shown in Fig. 2(c). The metal contacts were fabricated on each layer (D1 and D2 for WSe_2; S1 and S2 for MoS_2), see the bottom right of Fig. 2(c). When the metal electrodes D1 (WSe_2) and S1 (MoS_2) are coupled, the *p-n* junction is formed between the two 2D semiconductors. The natural *n*- and *p*-type channel characteristics of MoS_2 and WSe_2 are ascribed to the unintentional doping present in each 2D crystal. They observed a gate-tunable photovoltaic response from the I-V_{ds} curves of the junction in the gate range of −30 V to 30 V under white-light illumination, as shown in Fig. 2(d)-i. The colour plot of the photocurrent and the photocurrent map of the device are also shown in Fig. 2(d)-ii–iii.

Though 2D materials hold great promise in future electronics, the industrialization of 2D electronic devices faces many challenges. The major one is the development of controllable and stable doping of 2D semiconductors which must be overcome to realize both *n*-channel and *p*-channel FETs (two essential components for integrated electronics) just like those in traditional three-dimensional (3D) electronics based on silicon or GaAs. Moreover, a high-performance 2D FET requires a low contact resistance which can be achieved through degenerate doping in the contact region of 2D semiconductors. In addition, optoelectronic devices also require *p-n* junctions. As such, defect engineering is indispensable for tailoring carrier type and concentration of 2D electronic materials and then facilitate the realization of 2D devices. In addition to the beneficial facilitation of offering carriers, defects can also be detrimental for device performance as they also can act as undesirable carrier traps, or scattering center, or nonradiative recombination centers. A representative case is the significantly lower electron mobility of MoS_2 reported in experiments than that in theoretical limit, which mainly points to the mid-gap states induced by defects [47,48]. In fact, 2D materials should be viewed as real materials with defects, rather than perfect 2D layer from the perspective of thermodynamics [49]. Therefore, enhancing our knowledge on the defect physics of 2D semiconductors should advance the development of low-power, high-integration electronic devices based on them. The intentional electronic-properties control for conduction type and conductivity is mainly achieved by engineering point defect (for example vacancy, substitution, and interstitial). It should be noted that some large-scale defects such as grain boundary, dislocation, and edges, which may exist in chemically synthesized 2D materials, also influence the electronic properties of the materials [50]. For example, Zhou et al. [51] discovered two types of 60°grain boundaries in MoS_2, which introduce dispersive bands crossing the Fermi level of no-defect MoS_2 and then serve as perfect one-dimensional metallic quantum wires. In this review, point defects and their influence on the material properties and device performances are mainly concentrated on.

In this review, we will focus on the recent developments of point defect study in 2D semiconductors and their roles on engi-

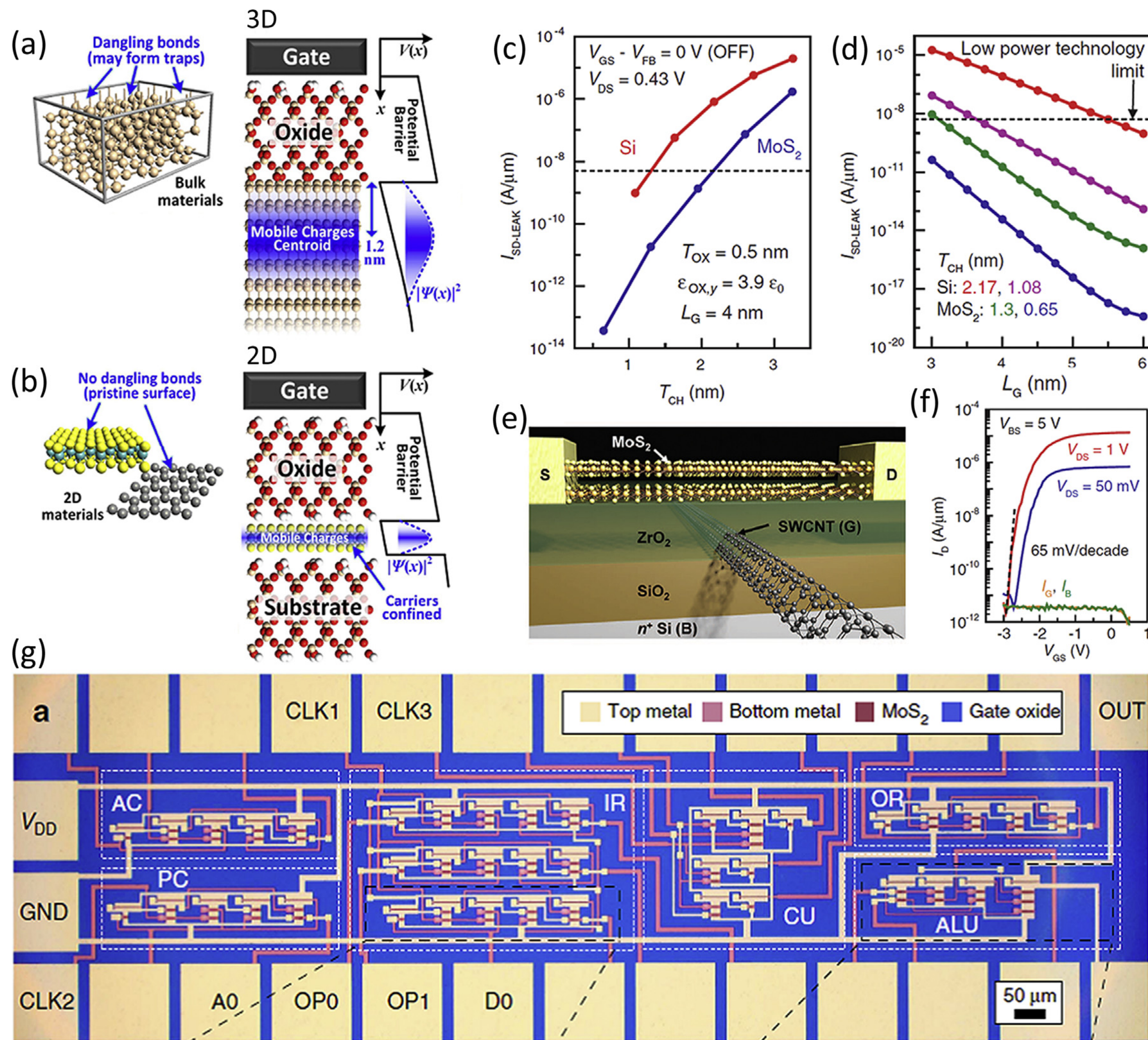

Fig. 1. Advantages of 2D semiconductors compared with 3D semiconductors for FETs. Schematic illustration of advantages of 2D materials compared with 3D materials for application in FETs: (a) left, 3D semiconductors with reduced thickness, right, gate electrostatics and mobile charge distribution in 3D materials. (b) left, 2D materials, right, gate electrostatics and mobile charge distribution in 2D materials. (c) source-to-drain leakage current $I_{SD\text{-}LEAK}$ in the OFF state with Wentzel-Kramers-Brillouin approximation as a function of channel thickness T_{CH} for silicon and MoS_2. (d) $I_{SD\text{-}LEAK}$ as a function of gate length L_G for silicon and MoS_2 with different T_{CH}. (e) Schematic of the FET with channel of bilayer MoS_2 and gate of single-walled carbon nanotube. (f) I_D-V_{GS} characteristics of the FET shown in (e). (g) Microscope image of the microprocessor consisting of 115 MoS_2 transistors. (a) and (b), reprinted with permission from Ref. [37], Copyright 2014, SPIE Journals and Proceedings. (c)–(f), reprinted with permission Ref. [27], Copyright 2016, AAAS. (g), reprinted with permission from Ref. [42], Copyright 2017, Nature Publishing Group.

neering 2D electronic devices. First, the identification of defects by experimental characterization, including atomic resolution imaging observed with electron microscope techniques and structural information probed by Raman and photoluminescence (PL) spectroscopy, is introduced. Second, the evaluation of defect properties, especially the ability to tune conductivity by two recent developed theoretical methods for carrier ionization from defect in 2D semiconductors, are clarified. Third, discussions of the role of defects in electronic device performance including carrier concentration, carrier type, carrier mobility, subthreshold slope, and contact resistance, are presented. Fourth, a database including some decisive characteristics of frequently studied defects in popular 2D semiconductors is summarized for references. Finally, we conclude the review with an outlook for the potential challenges and future direction of 2D electronics engineered by semiconductor defects. The present review should be useful for the electronic engineering community and scientists in other field work together to enable the making and modelling of 2D materials to result in the manufacture of electronic device.

Experimental characterization of defect

Atomic resolution imaging

Characterization of atomic structures of defects are foundations for the exploration of defect behaviors. Knowledge from atomic resolution imaging of defects is benefit for understanding of the material's properties. Transmission electron microscopy (TEM) and scanning tunneling microscopy (STM) are two main characterization tools, furthermore the TEM with equipped aberration corrector (AC) have realized atomic resolution [52]. In fact, the nature of down-scaled dimensions in 2D semiconductors enables more straightforward insights into atomic structure by the TEM or STM technique. Here, several typical 2D semiconductors are taken as examples to review the identification of their point defects with AC-TEM or STM. For example, Jin et al. [53] distinguished individual boron and nitrogen atoms and resolved the intrinsic defects in monolayer BN by high-resolution TEM (HRTEM). The electron beam irradiation preferentially removes boron atoms resulting in formation of boron vacancies as shown in Fig. 3(a)-i. Accompanied with

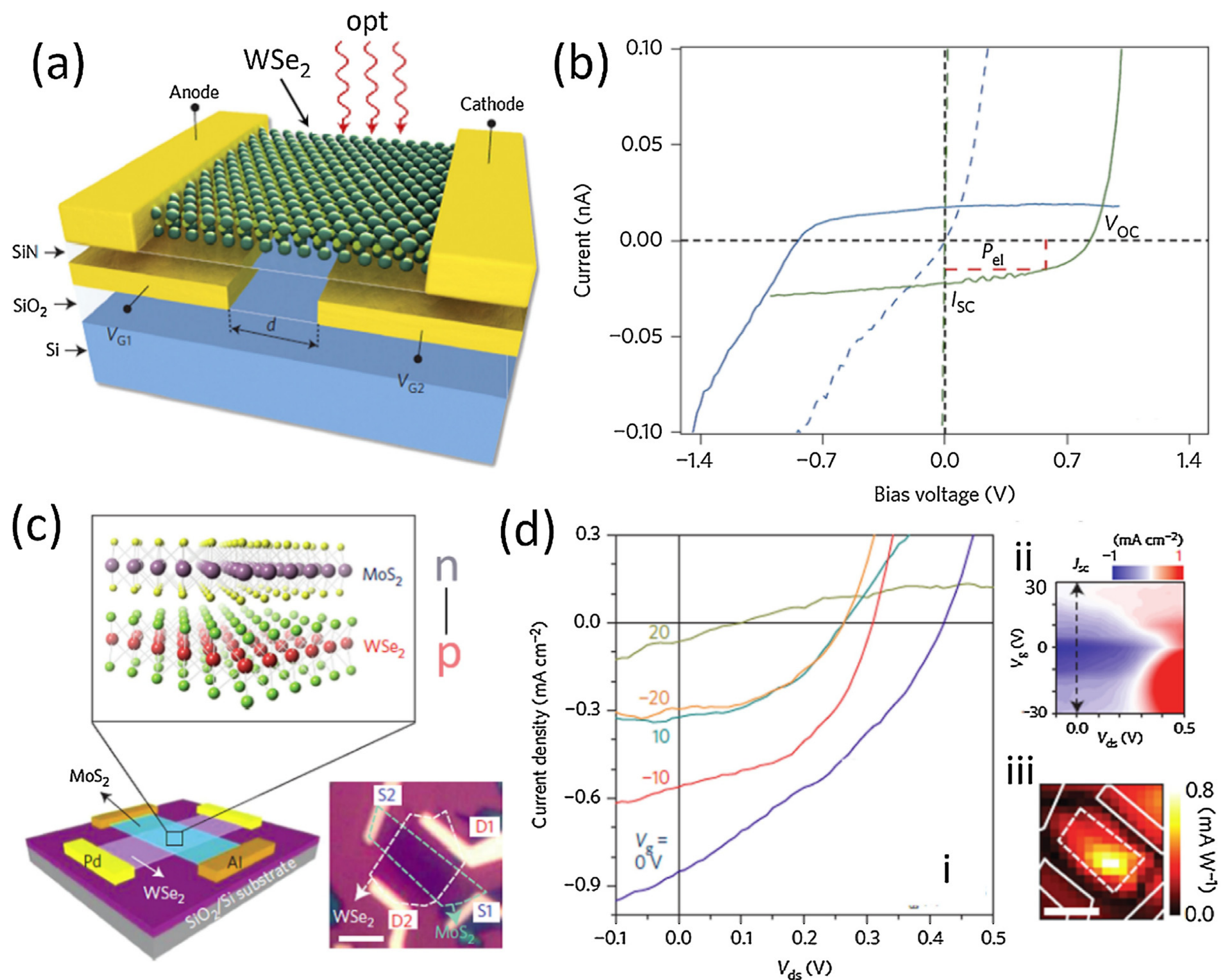

Fig. 2. *p-n* junction based on 2D semiconductors. (a) Schematic of the WSe2 *p-n* junction device. Two splitting electrodes are coupled to different regions. Biasing one gate with a positive voltage and the other with a negative voltage draws electrons and holes into the channel respectively, and thus a *p-n* junction is realized. (b) I–V characteristic of the *p-n* junction (V_{G1} = −40 V, V_{G2} = 40 V, green solid line) under optical illumination with 1400 Wm^{-2}. Other lines are for different biasing conditions. (c) Bottom left, schematic diagram of a van der Waals heterojunctions. Top, atomic structures of MoS_2 and WSe_2. Bottom right, optical image of the device. D1 and D2 (S1 and S2) represent the metal contacts of WSe2 (MoS2). When the metal electrodes D1 (WSe_2) and S1 (MoS_2) are coupled, the *p-n* junction is formed between the two 2D semiconductors. (d)-i, Photoresponse characteristics at different gate voltages under optical illumination; (d)-ii, Color plot of the photocurrent as a function of voltages Vds (x axis) and Vg (y axis); (d)-iii, Photocurrent map of the device presented in (c). (a) and (b), reprinted with permission from Ref. [45], Copyright 2014, Nature Publishing Group. (c) and (d), reprinted with permission from Ref. [46], Copyright 2014, Nature Publishing Group.

boron vacancies, some larger vacancies in triangle shape are also discriminated. Krivank et al. [52] identified the atomic substitutions in liquid-phase exfoliated monolayer BN using annular dark-field (ADF) imaging in an AC scanning transmission electron microscope (STEM), including carbon substituting for boron/nitrogen and oxygen substituting for nitrogen, as shown in Fig. 3(a)-ii. Boron vacancies are also identified in bilayer BN (Fig. 3(a)-iii) and the resultant distortions with interlayer bonding are uncovered by Alem et al. [54].

Other examples are from the structurally complex TMDs [55,56]. Among them, the most popular MoS_2 has been experimentally synthesized by mechanical exfoliation, or chemical vapor deposition (CVD), or physical vapor deposition (PVD). Zhou et al. [51] employed AC-STEM to visualize the intrinsic structural defects including point defects, grain boundaries, and edges in monolayer MoS_2 grown by CVD. The commonly observed point defects are monosulfur vacancy V_S, disulfur vacancy V_{S2}, multivacancy V_{MoS3} (removing one Mo and its neighboring three S), and another multivacancy V_{MoS6} (removing one Mo and its neighboring three S pairs) as shown in Fig. 3(b)-i–iv. Among them, V_S is most frequently observed. This is consistent with the lowest theoretical formation energy of V_S. Meanwhile, antisite defects are occasionally found in CVD-grown MoS_2. Instead, according to the study by Hong et al. [57], antisite defects including Mo_S (one Mo substituting one S atom, see Fig. 3(b)-v) and Mo_{S2} (one Mo substituting two S atoms, see Fig. 3(b)-vi) are easily observed in PVD grown samples. They revealed that the dominant defect species of monolayer MoS_2 is sensitive to the growth method and changes from S vacancy in CVD and mechanical exfoliation samples to Mo antisites in PVD samples. Carrying out HRTEM experiments, Komsa et al. [58] showed that S vacancies including V_S and V_{S2} can be produced under a 80-kV electron beam irradiation. The further filling of the vacancy sites with other atomic species is also observed. For intentional doping, Lin et al. [59] demonstrated the successful doping of MoS_2 with Re and Au through STEM studies, as can be seen in Fig. 3(c)-i–ii. Re is identified to occupy Mo site whereas Au preferably adsorbs on top of Mo, S, or the hollow center. For other candidates in the TMD family, in Nb-doped WS_2 Gao et al. [60] identified the position of Nb sitting at W site (see Fig. 3(d)) with AC-STEM. Cho et al. [61] studied the structural transition in monolayer $MoTe_2$ from semiconducting hexagonal phase to metallic monoclinic phase. The transition is driven by Te vacancy, which is also observed by STEM, see Fig. 3(e). Recently, a new member of the TMDs family, $PtSe_2$ also receives significant attention. Wang et al. successfully fabri-

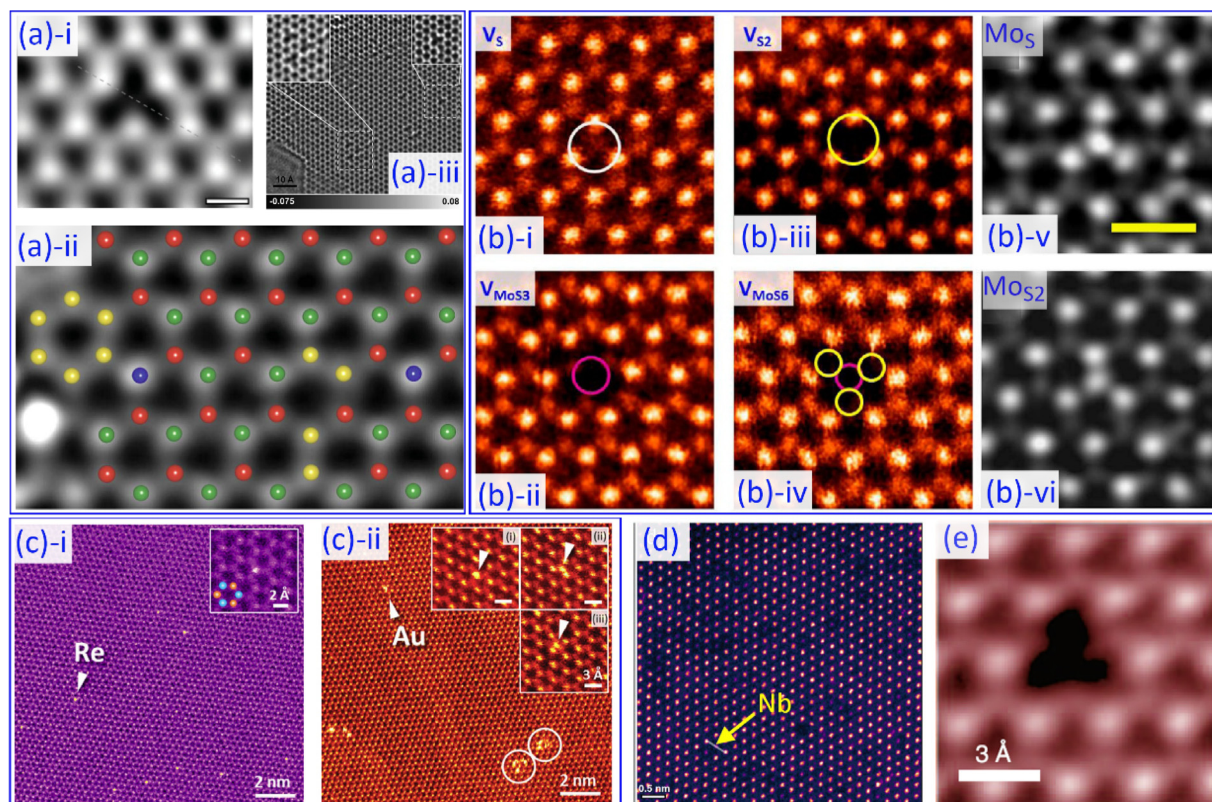

Fig. 3. Imaging of defects in 2D materials. (a)-i, HRTEM image of boron vacancy in monolayer BN; (a)-ii, TEM image of boron vacancy in bilayer BN; (a)-iii, ADF image of BN doped by C and O. Red: B; green: N; yellow: C; blue: O. (b)-i–v, STEM-ADF images of intrinsic defects (V_S, V_{S2}, V_{MoS3}, V_{MoS6}) in CVD-synthesized MoS_2; (b)-v–vi, STEM-ADF images of intrinsic defects (Mo_S, Mo_{S2}) in PVD-synthesized MoS_2. (c)-i and (c)-ii, ADF image of Re-doped and Au-doped MoS_2. (d) AC-STEM image of Nb-doped WS_2. (e) STEM image of Te vacancy of $MoTe_2$. (a)-i, reprinted with permission from Ref. [53], Copyright 2009, American Physical Society. (a)-ii, reprinted with permission from Ref. [52], Copyright 2010, Nature Publishing Group. (a)-iii, reprinted with permission from Ref. [54], Copyright 2011, American Physical Society. (b)-i–iv, reprinted with permission from Ref. [51], Copyright 2013, American Chemical Society. (b)-v–vi, reprinted with permission from Ref. [57], Copyright 2015, Nature Publishing Group. (c)-i–ii, reprinted with permission from Ref. [59], Copyright 2014, Wiley Publishing Group. (d), reprinted with permission from Ref. [60], Copyright 2016, Wiley Publishing Group. (e), reprinted with permission from Ref. [61], Copyright 2015, AAAS.

cated the monolayer 1T $PtSe_2$ film on a Pt (111) substrate by direct selenization [62]. On that basis, Lin et al. [63] demonstrated that a $PtSe_2$ monolayer can be grown in the form of a triangular pattern of alternating 1T and 1H phases. The phase transformation from semiconducting 1T to metallic 1H is also defect-assisted (by Se vacancy), which is observed by STM. The intrinsically-grown patterned 2D materials potentially provide ideal semiconductor-metal junctions for electronic devices. These characterizations described above straightforwardly confirm the existence of various defects in 2D materials.

Raman and photoluminescence spectroscopy

Raman spectroscopy is a popular nondestructive-and-efficient tool to detect defects in 2D materials according to the fingerprints of vibrational signals [64]. One of such cases is the well-known defect-related D and D' peaks of graphene probed by Raman spectroscopy [65]. Another example is that perfect monolayer MoS_2 has two prominent Raman-active peaks denoted as E' and A_1' [64,66,67]. The E' mode originate from the opposite in-plane vibrations of Mo and S atoms (namely, in-plane vibrations of two Mo-S bonds). The A_1' mode corresponds to out-of-plane vibrations of the Mo-S bonds with static center Mo atoms. Parkin et al. [66] observed the evolution of the Raman modes with varying amounts of S vacancy induced by electron beam irradiation. They found that when S vacancies are induced, the peaks of E' and A_1' behave redshift and blueshift, respectively, see Fig. 4(a). The frequency difference between E' and A_1' almost increases linearly with increasing S vacancy concentration, as shown in Fig. 4(b). The removal of top S atom leads to in-plane vibration of only one Mo-S bond, and consequently weaker restoring force constant and lower E' phonon frequency (redshift). For A_1', the missing Mo-S bond activates the out-of-plane vibration of originally static Mo atom and thus rises the frequency (blueshift). Nipane et al. also witnessed the significant broadening of E' peak in MoS_2 flake during the process of phosphorus implantation, which indicates the damage of the flake [67]. In addition to the changes of the E' and A_1' peaks, Mignuzzi et al. also observed some new defect-activated Raman peaks in Mn^+-bombarded MoS_2, as shown in Fig. 4(c) [68]. These peaks correlates with Brillouin-zone-edge phonons, which may be activated by the momentum contribution of defects. The most prominent peak at 227 cm^{-1} is attributed to the LA phonons with momentum $q \neq 0$ (at M point). The similar modes at zone edge also appear in WSe_2 with defects [69].

Besides, photoluminescence (PL) spectroscopy can be also used to obtain defect-related information. Defects can usually act as traps for carriers or excitons with introducing mid-gap states, which significantly influence the electronic and optical properties of the host materials [64]. Radiative recombination of the excitons bound to defects will lead to light emission, which can be captured by PL spectroscopy. For example, Wu et al. [70] employed electron beam irradiation to produce defects in WSe_2 (Fig. 4(d)) and observed the PL emission signals of the irradiated specimen and the pristine one at a low temperature (83 K) in Fig. 4(e). The pristine WSe_2 exhibits two PL peaks X_0 and X^+, which originate from the emissions of excitons and trions, respectively. However, the irradi-

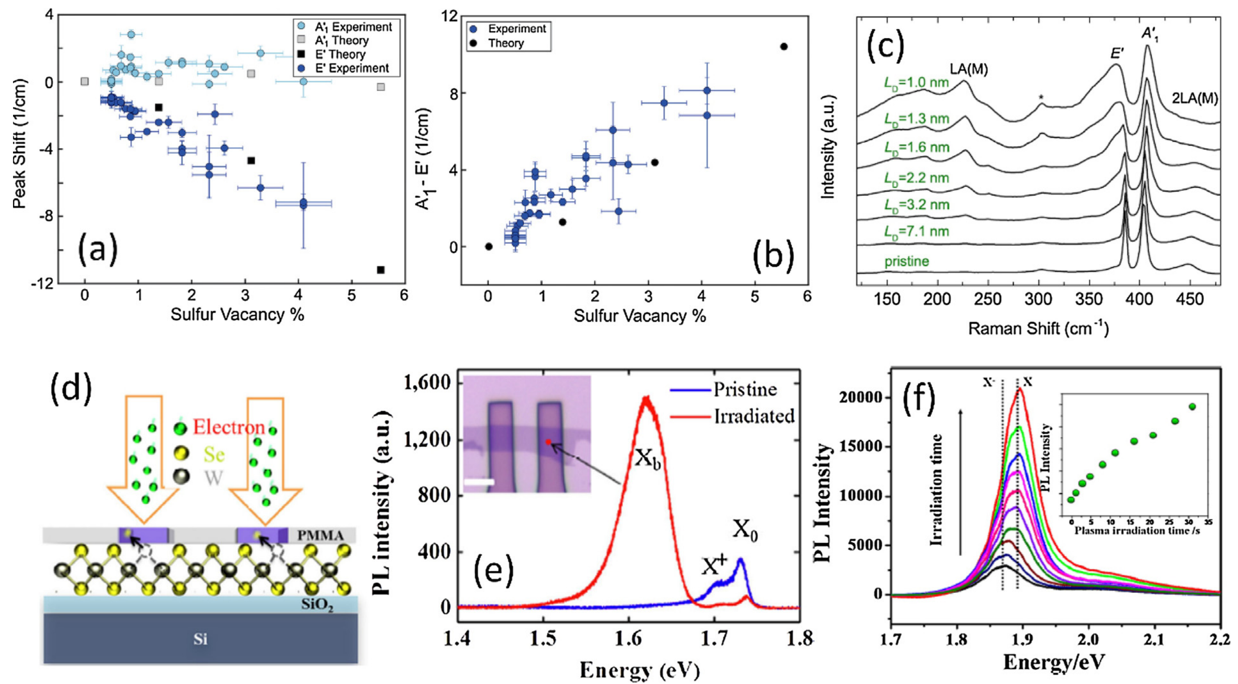

Fig. 4. Spectroscopic characterizations of defects in 2D materials. (a) Raman peak shift of E' and A_1' as a function of sulfur vacancy in monolayer MoS_2. (b) Frequency Difference between E' and A_1' Raman modes as a function of sulfur vacancy. (c) Raman peaks of monolayer MoS_2 with varying inter-defect distance L_D. (d) Schematic diagram of electron beam irradiation on WSe_2 sample and (e) PL spectroscopy of the pristine monolayer WSe_2 and the monolayer WSe_2 after irradiation. (f) PL spectra of monolayer MoS_2 after oxygen plasma irradiation with different durations. (a) and (b), reprinted with permission from Ref. [66], Copyright 2016, American Chemical Society. (c), reprinted with permission from Ref. [68], Copyright 2015, American Physical Society. (d) and (e), reprinted with permission from Ref. [70], Copyright 2016, Tsinghua University Press and Springer-Verlag Berlin Heidelberg. (f), reprinted with permission from Ref. [75], Copyright 2014, American Chemical Society.

ated sample have another new PL peak, named X_b, which is assigned to the emissions of excitons bound to some structural defects. They also found that the intensity of X_b vanishes with increasing temperature. This is because that the binding between defects and excitons is not strong enough to resist thermal perturbation. The X_b peak has been also observed in defective MoS_2. Defects can also be used to manipulate optical properties of 2D materials. For example, the monolayer MoS_2 has a direct bandgap which means a strong PL intensity. However, the measured PL intensity of as-prepared MoS_2 is below expectation. Mak et al. [71] showed that the weak PL is mostly ascribed to the formation of negatively charged excitons, i.e. trions (two electrons and one hole) in the naturally *n*-type MoS_2. The PL of MoS_2 can be enhanced by molecular adsorption or electrical gating with switching trions to excitons [72–75]. Nan et al. [75] realized the switch by defect engineering. Through O plasma irradiation, O adsorbed on the defect sites (such as the observed monosulfur vacancy) of MoS_2 and induced hole doping, which can deplete the original electron doping. The depletion of excess electron can convert trion to exciton and then result in strong enhancement of PL, as shown in Fig. 4(f). The results above also confirm the existence of defects in 2D semiconductor in terms of optical spectroscopic characterization.

Theoretical evaluation on carrier ionization energy of defect for conductivity

Many solid evidences of existing various defects in 2D semiconductors promote the exploration of their characteristics. Among them, the most critical performance for electronics is the ability to supply carriers by defect or impurity because it determines the conductive type and strength [76–80]. This ability can be evaluated by a specific physical quantity, i.e. ionization energy, which here is the energy required to free electrons or holes in defect levels to conduction band minimum (CBM) or valence band maximum (VBM). The defects with small ionization energies are likely to be thermally ionized to supply carriers at room temperature and thus are most desirable for semiconductors to tailor electrical conductivity. In contrast, the defects with large ionization energies are undesirable as they are ionized so infrequently that their contribution to the free carriers can be neglected. Worse, these deep defect states (with large ionization energy) usually play roles in carrier traps or nonradiative recombination centers. Usually, ionization energy can be analyzed from a ground-state electronic structure of defect or defect transition level with first-principles calculations, see the discussion below in detail.

Ionization energy (evaluated by ground-state electronic structure)

By examining the ground-state electronic structure, namely the single-particle energy levels of the electronic density of states (DOS) or band structure, the carrier type and ionization energy can be determined. The occupied or half-occupied single-particle levels of defect can donate electrons to CBM resulting in *n*-type conductivity, and the unoccupied or half-occupied single-particle levels can accept electrons from VBM resulting in *p*-type conductivity. The energy difference between single-particle level and corresponding band edge determines the ionization energy. If the single-particle levels are close to CBM/VBM for *n*-type/*p*-type defects (small ionization energy), the levels are expected to be shallow and the defects are expected to be ionized easily. On the contrary, the levels are supposed to be deep and the defects are supposed to hardly be ionized (large ionization energy).

So far there have been lots of studies reporting the electronic structure of defective 2D semiconductors, especially BN, MoS_2 and black phosphorus. For example, Huang et al. [81] systematically studied the electronic structures of vacancy defects and C substitution in single-layer BN. For the dominant defect of B vacancy (V_B), the removal of a B atom will induce one spin-up polarized

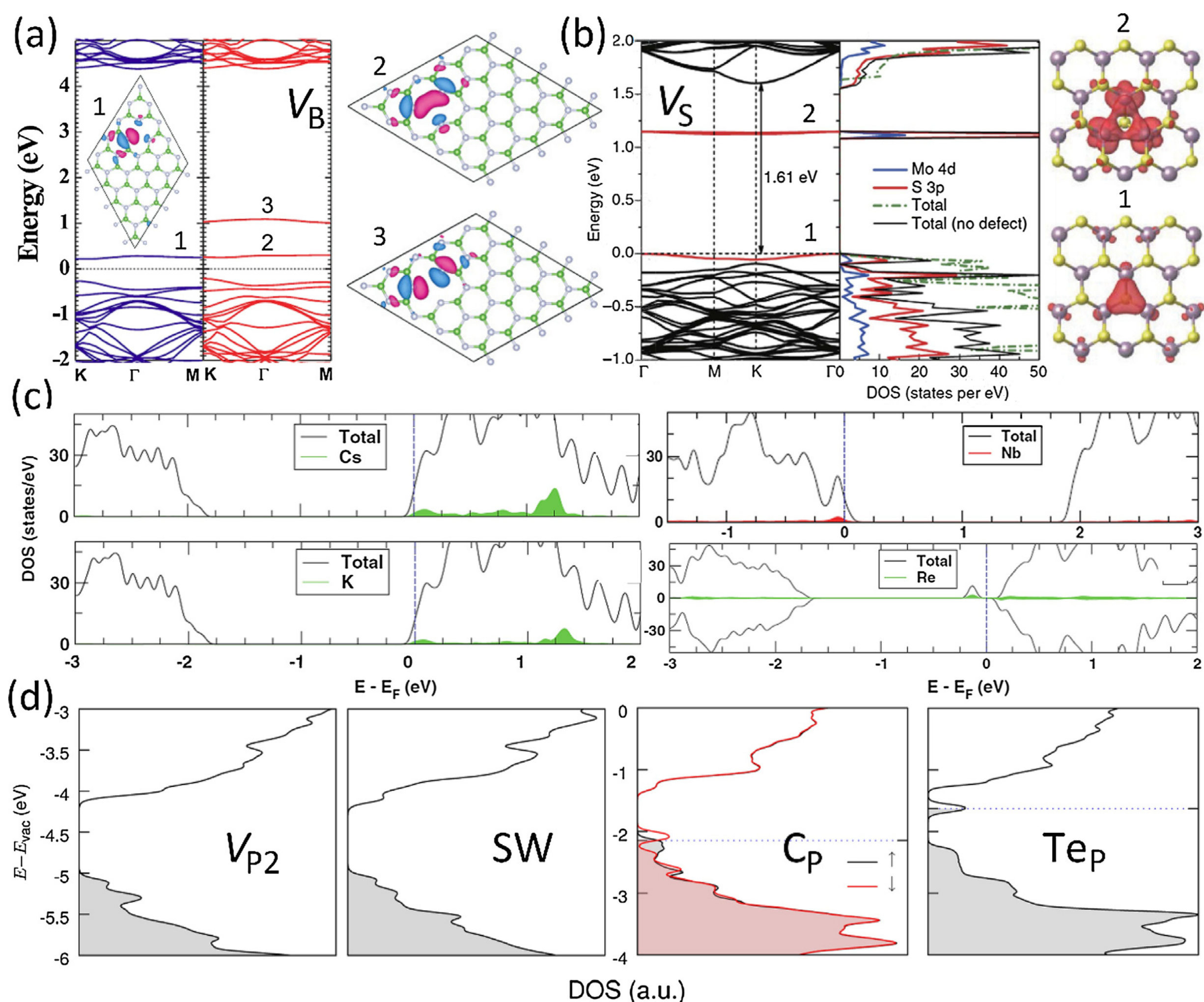

Fig. 5. Ground-state electronic structure of defects in 2D materials. (a) Spin-polarized band structure of boron vacancy (V_B) and Γ-point wave functions of the gap states labeled as 1, 2, and 3. Fermi level is set at 0 eV. (b) Band structure and DOS of monolayer MoS_2 with sulfur vacancy (V_S) and wave function of the gap states labeled as 2 and 1. Fermi level is set at 0 eV. (c) (left) DOS of Cs-adsorbed and K-adsorbed MoS_2; (right) DOS of Nb-doped and Re-doped MoS_2. Fermi level is set at 0 eV. (d) DOS of intrinsic defects including divacancy (V_{P2}) and Stone-Wales (SW), and substitutional defects including C and Te dopants in monolayer black phosphorus. The shadow regions represent filled states. For spin-polarized systems, the two spin states are shown in different colors. (a), reprinted with permission from Ref. [81], Copyright 2012, American Physical Society. (b), left: reprinted with permission from Ref. [47], Copyright 2013, Nature Publishing Group; right: reprinted with permission from Ref. [82], Copyright 2014, American Physical Society. (c), reprinted with permission from Ref. [84], Copyright 2013, American Physical Society. (d), reprinted with permission from Ref. [85], Copyright 2014, American Chemical Society.

level and two spin-down polarized levels within the bandgap, see Fig. 5(a). According to their wavefunctions, the defect levels all originate from the *p* orbitals of nearby N atoms around V_B. As the levels are all unoccupied, V_B thus can behave as an acceptor.

For MoS_2, the electronic structures of its native defects have been reported by a number of studies, such as the most popular sulfide vacancy, V_S [47,57,82,83]. V_S can generate three levels within the bandgap, see Fig. 5(b) [47]. The empty levels marked as 2 are doubly degenerated and the occupied level labeled as 1 is singlet. Levels of 2 and 1 are acceptor and donor states, respectively. Both of them are seemingly to be deep as acceptor level is far away from VBM and the donor level is away from CBM. To explore the possible *n*-type and *p*-type doing strategies of MoS_2, Dolui et al. performed a systematic investigation on the electronic structures of doped MoS_2 [84]. The dopants include transition metals (Y to Cd with exception of radioactive Tc, which is replaced by Re), alkali metals (Li, K, and Cs), nonmetals (H, N, P, and As), halogens (F, Cl, Br, and I), and molecular ions (NH_4^+ and BF_4^-). The doping sites include substitutional doping at both Mo and S site, as well as doping by adsorption. The promising *n*-type and *p*-type doping are alkali adsorption and Nb substitution at Mo site, respectively. As can be seen in Fig. 5(c), there is no obvious states within the bandgap induced by Cs adsorption and the DOS projected over Cs spread widely in the conduction band (over 1.5 eV). The situations of K and Li adsorption are similar. This means that alkali metals adsorbed on a MoS_2 monolayer can act as good *n*-type donors. For Nb substitution, Nb lack one electron than Mo, the Fermi energy shifts below the VBM. Beyond that, the DOS modifies slightly after the inclusion of Nb as shown in Fig. 5(c). All these mean that Nb may be a promising *p*-type dopant in MoS_2. In constrast, they showed that all substitutions studied do not possibly contribute to the effective *n*-type doping as the donor levels are found to be deep inside the band gap. Fig. 5(c) shows the DOS of Re substitution at Mo site, the excess electron of Re occupies the spin-up state, which is 0.3 eV below CBM.

In general, defects introduce states within the bandgap which strongly affect the properties of materials, just like those described above. These defects are classified as electronically active defects. Some defects, however, are electronically inactive with no introduction of gap states. These defects can only exist in neutral state. Liu et al. [85] proposed that most defects in black phosphorus

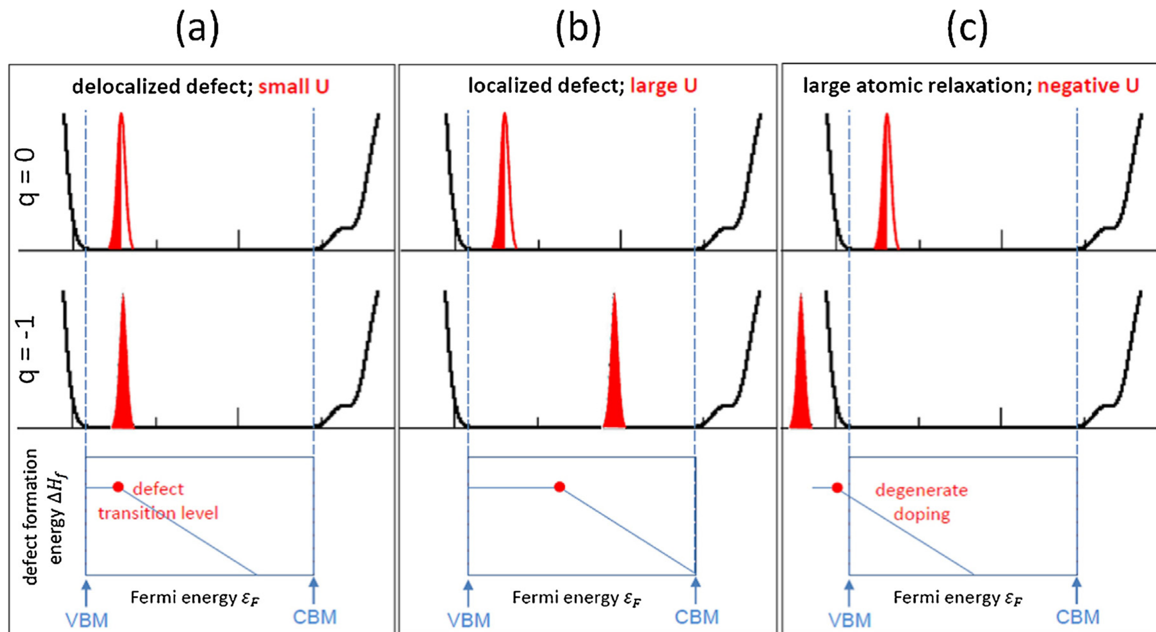

Fig. 6. Difference between single-particle level and transition level. Taking half-occupied acceptor state as example, schematic comparison of defect state given by DOS in neutral (q = 0) and charged states (q = −1) and transition level for (a) delocalized defect, (b) localized defect, and (c) defects with large atomic relaxation when charge state changes from (0) to (−1). The red shadows represent filled states.

including native defects and grain boundary are electronically inactive. The primary intrinsic defect are divacancy (V_{P2}) and Stone-Wales (SW, forming two pentagons and two heptagons through bond rotation on the basis of divacancy). Both of them do not induce gap states as shown in Fig. 5(d) because of their fully saturated bonds. The doped black phosphorus with foreign atoms are also studied. Substitutional C and Zn, and adsorbed K are predicted to be good *n*-type dopants whereas substitutional Te is not a proper *p*-type dopant according to the positions of single-particle defect states relative to corresponding band edges represented in DOS. The cases of C and Te can be seen in Fig. 5(d).

The difference between single-particle levels and transition levels

In addition to the single-particle level described above, ionization energy can also be determined by transition level. Transition level is defined by the Fermi energy at which two different charge states of one defect has the same formation energy [86,87]. The energy difference between transition level and CBM/VBM determines the donor/acceptor ionization energy. Above knowable, the position of single-particle level or transition level is required to evaluate ionization energy. Fig. 6 schematically describes the difference between single-particle levels and transition levels in term of acceptor. The ground-state (q = 0) DOS shows that the half-unoccupied single-particle levels locates above but near VBM, which means a relatively shallow acceptor. In fact, the single-particle picture does not consider the charged state (q = −1) in which one electron is added to the single-particle level after ionization. This means that the resulting Coulomb repulsion interaction (denoted by U) between the original electron and the new-added electron, and the corresponding atomic relaxation due to variation of charged states are ignored. However, they are all involved in the determination of transition level by the total energy calculations of different charged states. For defect with a delocalized wave function, the U is small so that the additional electron changes little the structure of defect and thus its level after ionization. As such, the defect transition level is almost in line with the ground-state single-particle level in DOS, see Fig. 6(a). However, for a defect with a localized wave function, the large Coulomb repulsion (+U) will raise the defect energy level of q = −1. Hence, the defect transition level will move to a position higher than the single-particle level of q = 0. Consequently, a disagreement between them can be seen in Fig. 6(b). In addition, for some defects, atoms can relax drastically to lower energy when the state of defect changes from (0) to (-1). The reduction of energy can be regarded as a negative Coulomb repulsion (-U). This usually make the single-particle level of q = −1 lower than that of q = 0. The negative-U systems is usually achieved by Jahn-Teller distortion [88,89]. In such case, the defect transition level should locate below the energy level of q = 0 and sometimes even below VBM, see Fig. 6(c). Therefore, transition level can give more accurate evaluation on ionization energy of defect and the ability to supply carriers. In fact, transition level has significantly contributed to explore many microscopic origin of doping limits and overcome the doping difficulty in 3D semiconductors, especially for group-III nitrides and II–VI compounds [76,90–93]. Also, it play a very important role in elucidating the origin of PL emission peaks of group-III nitrides [94–96].

Ionization energy (evaluated by transition level)

As mentioned, ionization energy can be determined by transition level through the calculations of formation energies of defects in their neutral and charged states. Generally, first-principles defect calculations require to invoke periodic boundary conditions, in which charged defects form an infinitely periodic array [76,97]. To deal with the artificial long-range Coulomb interaction between charged defects and its images, a homogenous counter charge (Jellium background) must be added to neutralize the calculated cell [76,97]. Wang, Li, and Zhang et al. [98] found that although the scheme works well for traditional 3D semiconductors, it encounters an energy divergence for charged defects in 2D materials. The divergence originates from the strong Coulomb interaction between charged defects and Jellium charges. As shown in Fig. 7(a), the distribution of ionized carriers in real situation and Jellium charges are similar for 3D systems but completely different for 2D systems. Taking 2D BN and 3D cubic BN as examples, the charged forma-

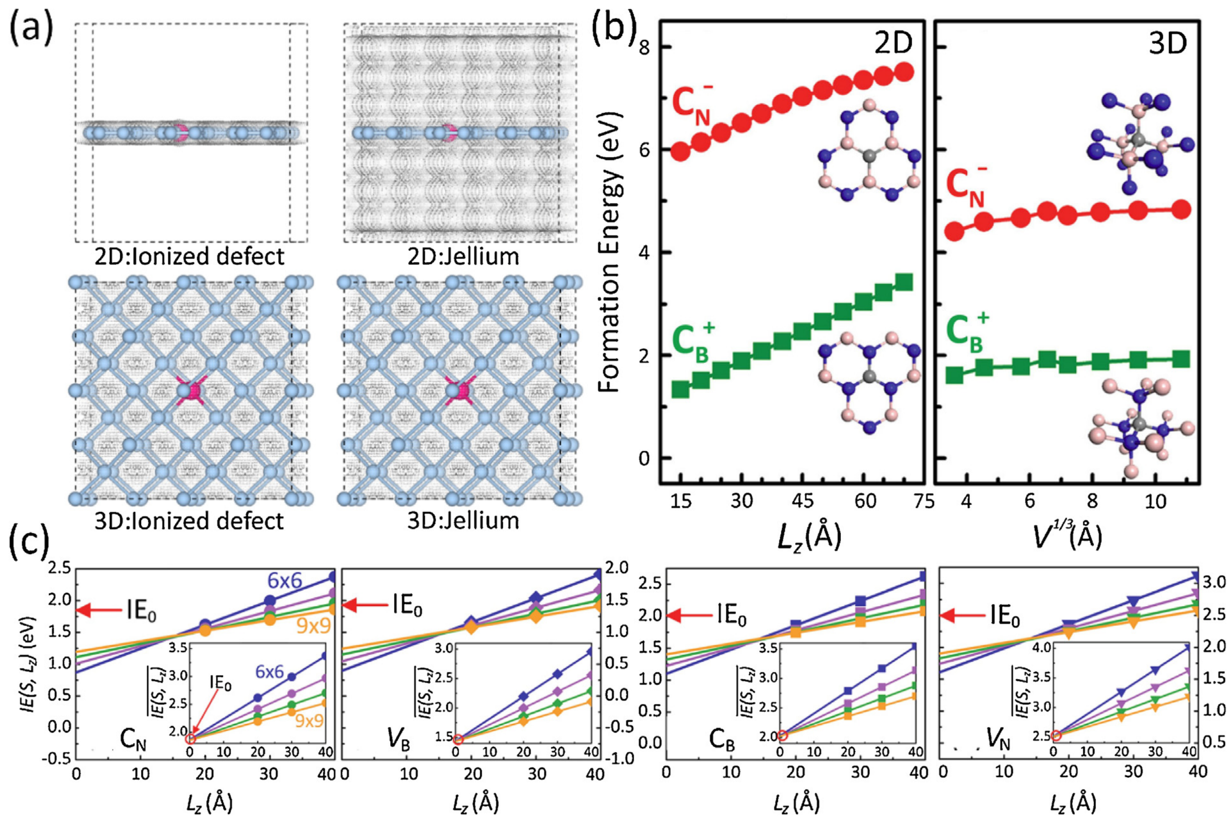

Fig. 7. Evaluation difficulty and method of charged defects in 2D materials. (a) Schematic diagram of carrier distribution in real defect ionization and Jellium charge distribution in Jellium approach of 3D and 2D materials. (b) Formation energies of charged C_B^+ and C_N^- in 2D BN and 3D BN. Insets show corresponding local structures of C_B (C replace B) and C_N (C replace N). (c) Ionization energiesof C_N and V_B (B vacancy), C_B and V_N (N vacancy) at different lateral size (S, 6 × 6 to 9 × 9) and vacuum size (L_z, 20 Å to 40 Å) (, where IE_0 is converged ionization energy). Insets show as a function of L_z. The converged IE_0s (red-circle highlight) are deduced from the insets at L_z = 0. Reprinted with permission from Ref. [98]. Copyright 2015, American Physical Society.

tion energies of C_B (C occupies B site, donor) and C_N (C occupies N site, acceptor) with varying cell size are calculated within the Jellium scheme, as shown in Fig. 7(b). It is clear that the charged formation energies of 3D BN gradually tend to convergent values with increasing cell size, however, those of 2D BN diverge linearly with increasing vacuum size L_z. These results reveal that the results of energy calculation of 2D charged defects based on such scheme can scatter widely if vacuum size L_z is arbitrarily chosen. To resolve the difficulty, Wang, Li, and Zhang et al. further derived an analytic expression for the asymptotic behavior of the Coulomb divergence, $IE(S, L_z) = IE_0 + \alpha/\sqrt{S} + (\beta/S)L_z$, which shows the converged energy in the limit of zero Jellium density (lateral area S → ∞) [98], see the explanation of the formula in the caption of Fig. 7. By extrapolating the expression, the converged energy can be readily obtained. Fig. 7(c) shows the converged ionization energies of defects of 2D BN, which are all unexpectedly deep, 1.86 eV for C_N, 2.03 eV for C_B, 1.44 eV for V_B, and 2.50 eV for V_N. They are much deeper than those of 3D BN, 0.18 eV for C_N, 0.00 eV for C_B, 0.37 eV for V_B, and 0.36 eV for V_N. They also identified the unphysical occupation of vacuum levels for all acceptors when the vacuum size is adequately large. The formulation combined with first-principles calculations can be used to determine energies of charged defects of all 2D materials and quasi-2D materials such as interfaces and surfaces. Application to one-dimensional charged systems is also straightforward with further extended expression. On the other hand, most recently, by using the extrapolation method proposed by Wang, Li, and Zhang et al. (WLZ extrapolation) [98], Ma et al. [99] demonstrated that substrate screening is an effective way to tune defect ionization energy for 2D semiconductors. Taking the Cl, Br, and I substitutions on S sites (X_S, X = Cl, Br, I) in MoS_2 an examples, they show that the ionzation energy decreases with enhanced substrate screening. For I_S, the ionization energy decreases from 0.63 eV for the freestanding MoS_2, to 0.39 eV when MoS_2 is on a SiO_2 substrate, further to 0.17 eV when MoS_2 is on a Al_2O_3 substrate.

Komsa et al. [100] proposed another finite-size supercell correction scheme for charged formation energies of defects at surfaces and interfaces. In this scheme, the correction term is the energy difference between the electrostatic energy of an isolated charge distribution and the same charge experiencing periodic boundary conditions. The implementation depends on a dielectric constant profile extracted from electronic-structure calculations, and a construction of a model Gaussian charge. Application the method to the native defects [101] (including vacancy, antisite, interstitial, and adatom) in monolayer MoS_2 reveals that S vacancy indeed has the lowest neutral formation energy which is consistent with the easy observation of Vs. However, V_S acts as a deep acceptor with ionization energy of 1.40 eV and thus cannot be attributed to the natural n-type conductivity in MoS_2, see Fig. 8(a) [101]. Meanwhile, the substitutional Re impurity, which naturally exists in MoS_2 samples is predicted to be a good n-type dopant. They also showed the comparison of transition levels of V_S and V_{Mo} (Mo vacancy) in monolayer MoS_2 and 3D bulk MoS_2 as calculated with PBE-D (Perdew-Burke-Ernzerhof and Van der Waals interaction correction) and HSE (Heyd-Scuseria-Ernzerhof) functionals, see Fig. 8(b) [101]. It can be seen that V_S and V_{Mo} in monolayer MoS_2 are substantially deeper than that in 3D bulk MoS_2. Also, HSE enlarges the bandgap and leads to deeper but more accurate defect levels. Due to the inherently weak screening, defects usually induce deep levels in 2D semiconductors as described above. However, the screening can be enhanced by dielectric environments surrounding the 2D mate-

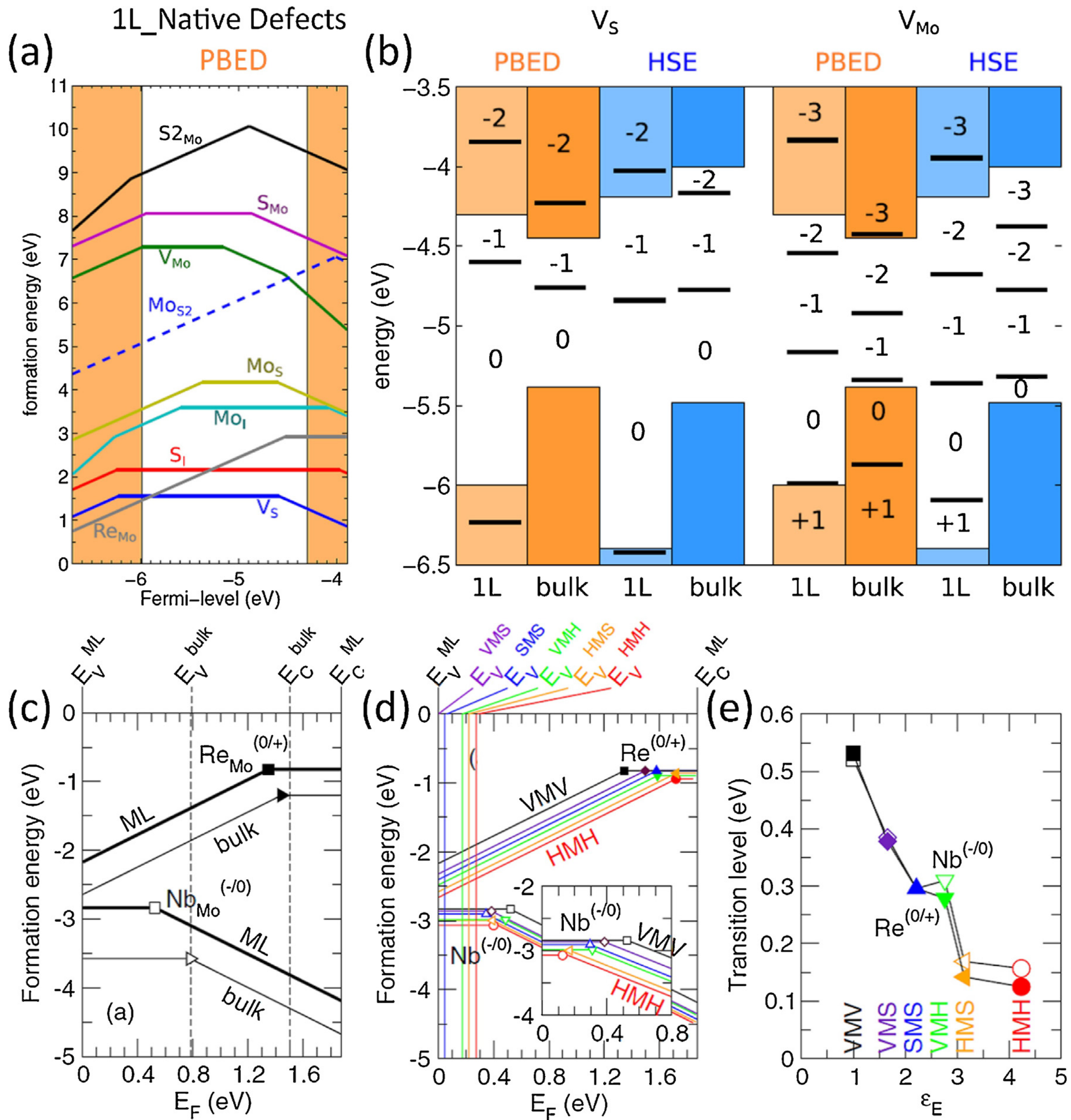

Fig. 8. Ionization energy evaluation of defects in 2D MoS_2. (a) Formation energies of native defects with PBE-D functional in monolayer MoS_2 as a function of Fermi level. (b) Transition level of S and Mo vacancy in monolayer MoS_2 and 3D bulk MoS_2 as calculated with PBE-D and HSE functionals. (c) Formation energies of Re_{Mo} and Nb_{Mo} in neutral and singly charged states in monolayer MoS_2 and 3D bulk MoS_2 as a function of Fermi level. (d) Formation energies of Re_{Mo} and Nb_{Mo} in neutral and singly charged states in Vacuum/MoS2/Vacuum (black), Vacuum/MoS2/SiO2 (purple), $SiO_2/MoS_2/SiO_2$ (blue), Vacuum/MoS_2/HfO_2 (green), $HfO_2/MoS_2/SiO_2$ (orange), and $HfO_2/MoS_2/HfO_2$ (red) systems as function of Fermi level. (e) Transition levels of Re_{Mo} and Nb_{Mo} as a function of the environmental dielectric constants. (a) and (b), reprinted with permission from Ref. [101], Copyright 2015, American Physical Society. (c)-(e), reprinted with permission from Ref. [102], Copyright 2015, American Physical Society.

rials. Noh et al. [102] used the same method proposed by Komsa et al. to study the effects of dielectric environments on the transition levels of Re and Nb (substitution at Mo site, Re_{Mo} and Nb_{Mo}) in monolayer MoS_2. As shown in Fig. 8(c), Re_{Mo} and Nb_{Mo} are found to be deep defects with transition levels of 0.53 eV below the CBM ($E_C^{ML} - 0.53$) and 0.52 eV above the VBM ($E_V^{ML} + 0.52$) in monolayer whereas they are shallow defects in 3D MoS_2 (Re_{Mo},$E_C^{ML} - 0.06$ and Nb_{Mo}, $E_V^{ML} + 0.00$). Further, various dielectric environments surrounding monolayer MoS_2 are considered, as shown in Fig. 8(d). MoS_2 is sandwiched between two dielectric layers. The defect transition levels are found to be shallower with increasing dielectric screening, in order of VMV, VMS, SMS, VMH, HMS, and HMH where V, M, S, H represent vacuum, monolayer MoS_2, SiO_2, and HfO_2, see Fig. 8(e). The results hint that for 2D semiconductors, the defect properties strongly depend on the environments surrounding the host layer material.

Both methods (WLZ extrapolation and Komsa correction) above provide important theoretical frameworks for evaluating the ability of defect to supply carriers in 2D semiconductors. In fact, Wang et al. [98] also compared the results obtained with the two methods. For C_N and C_B in monolayer BN, the ionization energies are 1.86 eV and 2.03 eV with the WLZ extrapolation [98] and are 2.03 eV and 2.24 eV with the Komsa correction [103]. To further confirm the reliability of the methods, Wang et al. [98] performed an additional benchmark calculation for C_B in very large supercells (lateral dimension $L_x \times L_y$ ranging from 15×15 to 19×19, atom number ranging from 450 to 722) with $L_x = L_y = L_z$. The direct extrapolation of the linear dependence in $1/L$ yields a limiting value of 2.13 eV,

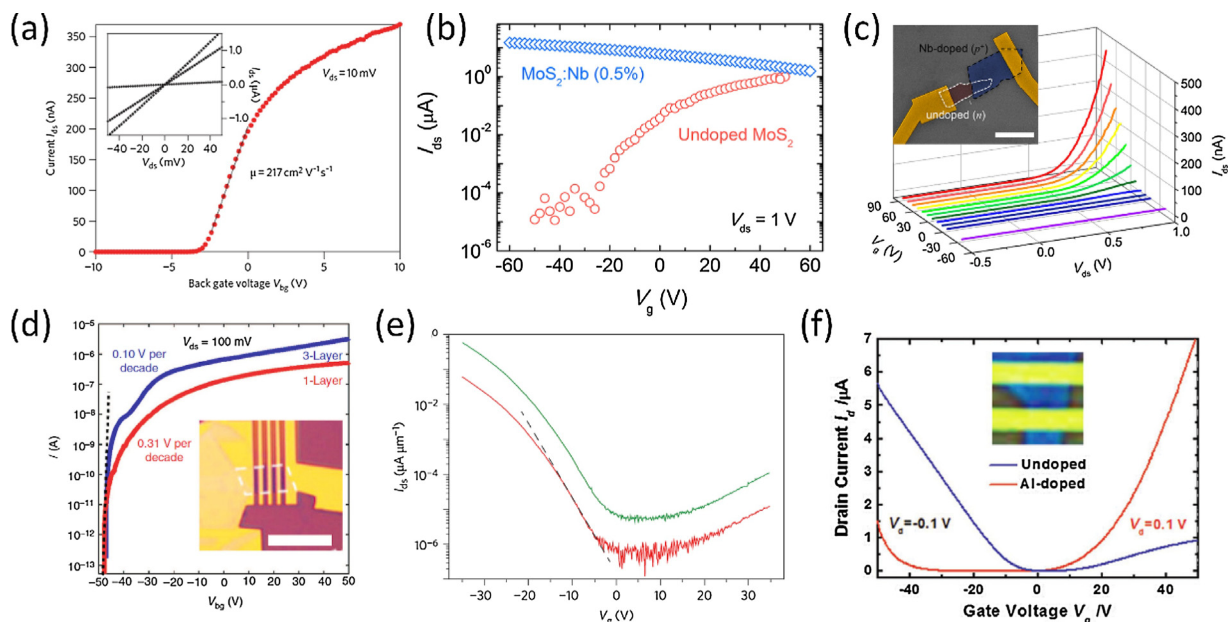

Fig. 9. Realization of *n*-type and *p*-type conductivity of 2D materials by defect engineering. (a) Room-temperature transfer characteristic of the FET based on monolayer MoS_2. (b) Gate voltage dependence of channel current of Nb-doped and undoped MoS_2. (c) Current-voltage characteristic at variable gate voltage measured across the *p*-*n* junction assembled with Nb-doped and undoped MoS_2. (d) Transfer characteristic of monolayer (red) and trilayer (blue) ReS_2 FET devices. (e) Source-drain current as a function of gate voltage from black phosphorus FET. (f) Comparison of the transfer characteristic for pristine and Al-doped black phosphorus FETs. (a), reprinted with permission from Ref. [28], Copyright 2011, Nature Publishing Group. (b) and (c), reprinted with permission from Ref. [107], Copyright 2014, American Chemical Society. (d), reprinted with permission from Ref. [108], Copyright 2015, Nature Publishing Group. (e), reprinted with permission from Ref. [23], Copyright 2014, Nature Publishing Group. (f) reprinted with permission from Ref. [109], Copyright 2017, Wiley Publishing Group.

which is nearly halfway between the two methods, namely both methods yield reasonably good agreement within ~0.1 eV.

Besides the two early methods above, some other works are also trying to correct the error in electrostatic energy of charged defect in 2D materials and quasi-2D materials. Vinichenko et al. [104] proposed an internally consistent approach for the energy calculations of charged defects in inhomogeneous and anisotropic dielectric environments, which is applicable for both 3D and 2D materials. Li et al. [105] presented a virtual ionic crystal (VIC) method wherein instead of Jellium background, an actual zero-dimensional species is induced to compensate a charged surface defect in a unit cell and then neutralize the cell. The energy required to charge a defect is derived from the energy of the unit cell and charge transfer quantity in VIC.

These methods described above substantially advance the defect physics in emerging 2D semiconductors by solving a critical problem, namely, to obtain a converged determination of charged defect energy. Further, this allows the accurate determination of ionization energy, which is tremendously important for 2D electronic devices because of its close relation with conductivity type and strength. In other words, these methods have significances in developing practical *n*-type and *p*-type doping strategy for 2D device applications.

Roles of defect in engineering 2D electronic devices

Realization of n/p*-type conductivity for devices by defect*

The applications of semiconductors in electronic device depend on their dopability. If one semiconductor cannot realize *n*-type and *p*-type conductivity in form of bipolar doping, it cannot not be used in FETs which is the building blocks for modern electronics. Furthermore, many optoelectronic device also require bipolar doping [106]. However, a natively unipolar doping propensity is usually found in traditional 3D semiconductors [76,106]. So far, FETs based on various 2D semiconductors have been achieved. Similar to 3D semiconductors, most 2D semiconductors are also found to have a natural tendency with one certain doping type. This can be identified by transfer characteristic measurements in FETs or Hall effect measurements. This natural conductivity in device originates from spontaneously formed native defects or unintentional impurities. Radisavljevic et al. [28] realized a FET with monolayer MoS_2 as channel material. The transfer characteristic of the transistor is shown in Fig. 9(a), which shows a clear *n*-type doping behavior. The FET features a room-temperature mobility of ~ 200 $cm^2V^{-1}s^{-1}$ and a current on/off ratio of 10^8. The natural *n*-type doping in MoS_2 has been observed by a number of studies and the origin usually points to the Re impurity natively existing in natural MoS_2 samples. In quest for bipolar doping for homogeneous *p*-*n* junctions, attention has been paid to explore *p*-type doping in MoS_2. Suh et al. [107] demonstrated a stable and degenerate *p*-type doping by incorporating Nb to substitute Mo in MoS_2, see the transfer characteristics in Fig. 9(b). They also fabricated a vertical *p*-*n* junction consisting of the Nb-doped and undoped MoS_2, which shows a good rectification characteristics as shown in Fig. 9(c). For other TMDs, ReS_2 also holds a native *n*-type doping propensity identified by the transfer characteristic of its FET, see Fig. 9(d) [108]. The *p*-type doping propensity has been found in black phosphorus. Li et al. successfully fabricated FETs based on few-layer black phosphorus with current on/off of 10^5 [23]. The carrier mobility is thickness-dependent with the highest value up to 1000 cm^2V^{-1} s^{-1}. The transfer characteristic of the FET shown in Fig. 9(e) reveals the natural *p*-type doping. Prakash et al. [109] reported the *n*-type FETs based on few-layer black phosphorus, which is achieved by Al adatoms doping. The comparison of transfer curve for FETs based on the undoped and Al-doped black phosphorus in Fig. 9(f) obviously shows respective *p*-type and *n*-type conductivity. In addition to the experimental reports, many theoretical studies have also made great efforts to explore possible *n*-type and *p*-type conductivity of 2D semiconductors through the calculations of ionization energy. To gain a systematic insight of

Table 1
Summary of carrier type, ionization energy, and carrier density of defects in typical 2D semiconductors from theoretical calculations or experimental measurements. In the second column, "V", "M", "S", "H" represent vacuum, monolayer, SiO_2, HfO_2, respectively. For example, VMV means freestanding monolayer material. In the third column, "V" means vacancy; "ad" means adsorption; "i" means interstitial; "A_B" means that atom B is replaced by atom A. In the final column, "Exp." represents experimental results, "TC" means transfer characteristics curve of FET device, "Hall" means Hall measurements, and "XPS" means x-ray photoelectron spectroscopy.

2D Semiconductor	Thickness/environment	Defect	Carrier type	Ionization energy (eV)	Technique
BN	VMV	V_B	p-type	1.44 [98]	Theory (ionization energy by transition level)
		V_N	n-type	2.50 [98]	
		C_B	n-type	2.03 [98]/2.24 [103]	
		C_N	p-type	1.86 [98]/2.03 [103]	
		C_{ad}	p-type	2.22 [103]	
			n-type	4.42 [103]	
		B_{ad}	p-type	3.13 [103]	
			n-type	3.32 [103]	
		N_{ad}	p-type	1.40 [103]	
			n-type	4.96 [103]	
MoS_2	VMV	V_S	p-type	1.70 [82]/1.40 [101]	
		V_{Mo}	p-type	1.10 [82]/0.85 [101]	
		Mo_i	n-type	1.55 [82]/1.30 [101]	
		Mn_{Mo}	n-type	3.89 [103]	
		F_S	n-type	3.65 [103]	
		Re_{Mo}	n-type	0.22 [101]	
	VMV	Re_{Mo} [102]	n-type	0.53	
	VMS			0.37	
	SMS			0.29	
	VMH			0.27	
	HMS			0.14	
	HMH			0.12	
	VMV	Nb_{Mo} [102]	p-type	0.52	
	VMS			0.38	
	SMS			0.29	
	VMH			0.30	
	HMS			0.16	
	HMH			0.15	
2D Semiconductor	**Thickness/environment**	**Defect**	**Carrier type**	**Carrier density**	**Technique**
MoS_2	Mono-Multilayer	Unintentional	n-type [46,107,122–125]	1.6×10^{12} cm^{-2} [124]	Exp. (TC)
	Multilayer	Nb_{Mo}	p-type	3×10^{19} cm^{-3} [107]	Exp. (TC, Hall)
	Few-layer	Nb_{Mo}		3.1×10^{20} cm^{-3} [126]	Exp. (Hall)
		P doping [67]		–	Exp. (TC, XPS)
		Chloride	n-type	2.9×10^{13} cm^{-2} [121]	
WS_2	Few-layer	Chloride	n-type	2.3×10^{13} cm^{-2} [121]	
	Monolayer	Unintentional	n-type [127]	–	Exp. (TC)
ReS_2	Monolayer, Trilayer	Unintentional	n-type [108]	–	Exp. (TC)
WSe_2	Monolayer	Unintentional	p-type [46]	–	
BP	Few-layer	Unintentional	p-type [23]	–	Exp. (TC)
		Cu_{ad}	n-type [128]	–	
		Al_{ad}	n-type [109]	–	
InSe	Multilayer	Unintentional	n-type [129,130]	–	Exp. (TC, Hall)
SnO	Multilayer	Unintentional	p-type [131]	–	Exp. (TC)

the dopability of 2D semiconductors, we provide a summarization table wherein the theoretically predicted carrier type and ionization energy, and experimentally achieved carrier type and carrier density of various defects in predominant 2D semiconductors are given as a database, see Table 1. It provides the reference information for developing practical n-type and p-type doping strategy of 2D semiconductors for 2D electronics. All the studies show that defect engineering is indispensable for the fabrication of 2D electronic devices.

Device performances associated with defects

Defects engineering not only plays an indispensable role in fabricating electronic devices but also an important role in affecting or optimizing device performance. Carrier mobility, subthreshold slope, and contact resistance of FET are often used as figures of merit for evaluating device performance [2]. The experimental mobility of monolayer MoS_2 on SiO_2 substrate at room temperature ranges from 0.1 to 55 cm^2V^{-1} s^{-1} [28,48,110,111], which is an order magnitude lower than the theoretically predicted phonon-limited mobility of 410 cm^2V^{-1} s^{-1} at room temperature [112,113]. Potential sources of the low mobility from the carrier scattering mainly include intrinsic defects as well as extrinsic charged impurities or substrate phonons. Qiu et al. carried out a systematic study on the carrier transport in MoS_2 [47]. As shown in Fig. 10(a), in perfect MoS_2, the electron density is periodic in real space and transport is band-like. In contrast, at low carrier density, the electrons are localized around defects in defective MoS_2 and their transport are through the hopping mechanism. As carrier density increases, a band-like transport can be expected. The measured conductivity as a function of temperature at various carrier density is shown in Fig. 10(b). In the high-temperature region, the conductivity increases quickly and can be fitted with the equation of $\sigma \sim exp(-T_0/T)$, which indicates a nearest-neighboring hopping transport mechanism. In the low-temperature region, the conductivity exhibits much weaker temperature dependence and can be well fitted by the variable-range hopping equation of $\sigma \sim \exp(-T_0/T)^{1/3}$. The localized states associated with hopping transport is ascribed to the commonly observed S vacancy [47].

Yu et al. showed that S vacancy can be repaired by (3-mercaptopropyl)trimethoxysilane (MPS) molecular doping under mild annealing in MoS_2, as shown in Fig. 10(c) [114]. Firstly, the MPS molecule chemically adsorbs onto the site of S vacancy of MoS_2 via its own S atom and then it sequentially cleaves the S-H bond and S-C bond. The final products are perfect MoS_2 and

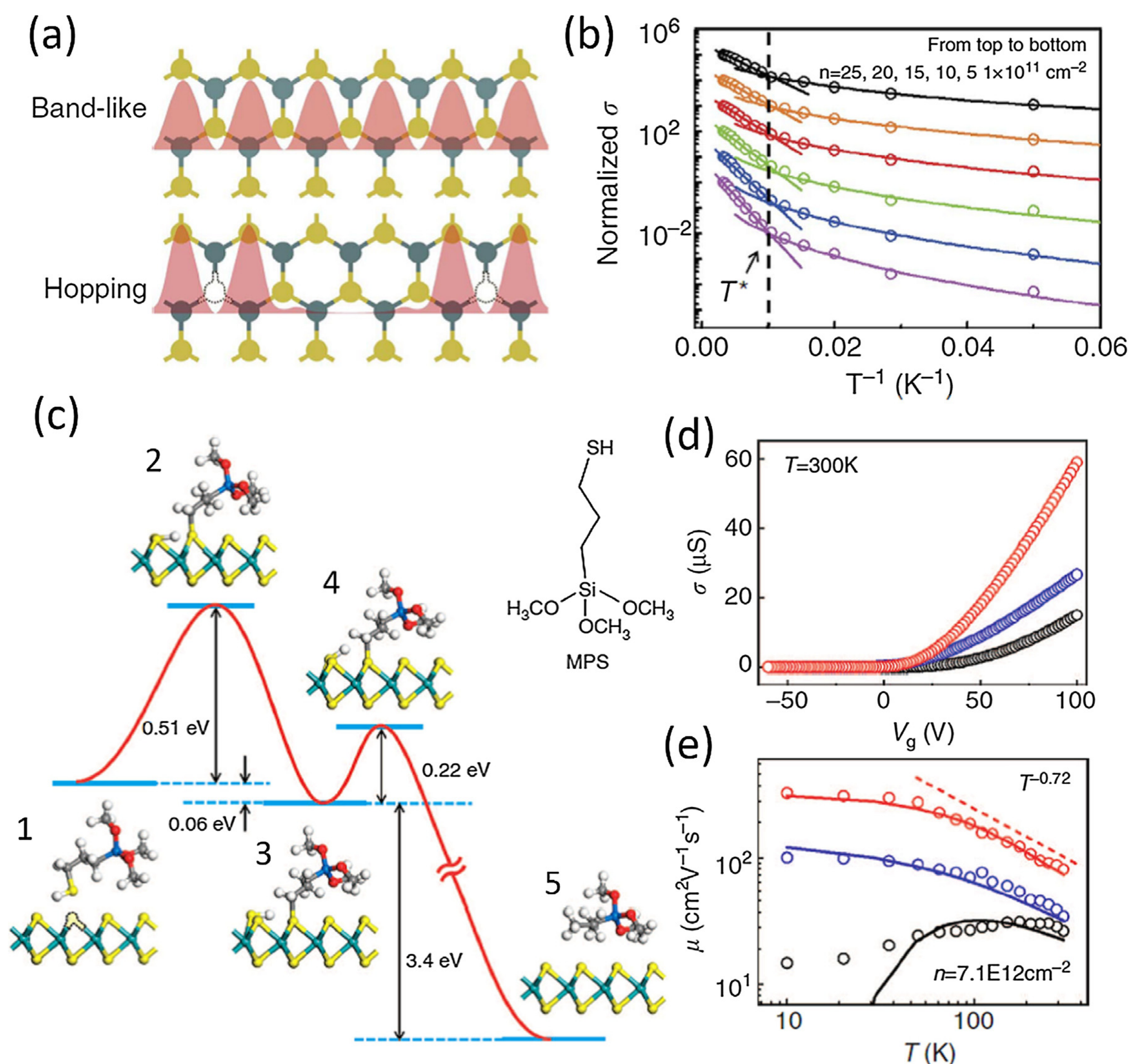

Fig. 10. Carrier hopping transport through defect states and improving carrier transport in MoS_2 by defect engineering. (a) Schematics of electron transport mechanisms in perfect and defective MoS_2. (b) Arrhenius plot of measured conductivity of MoS_2 as a function of temperature. (c) Kinetics and transient states of the reaction of S-vacancy repair of MoS_2 with MPS molecule. (d) and (e) Conductivity-gate voltage and mobility-temperature characteristic for as-exfoliated (black curve) MoS_2, single-side treated MoS_2 by MPS molecule (blue curve), and double-sides treated MoS_2 by MPS molecule (red curve). (a) and (b), reprinted with permission from Ref. [47], Copyright 2013, Nature Publishing Group. (c)-(e), reprinted with permission from Ref. [114], Copyright 2014, Nature Publishing Group.

trimethoxy(propyl)silane. The MoS_2 with both sides treated by MPS shows improved conductivity and mobility compared to the single-side treated one and untreated one, see Fig. 10(d) and (e).

Another route to improve mobility is to reduce extrinsic defect effect, such as the charged impurities scattering. It is found that the mobility of MoS_2 increase to 200 $cm^2V^{-1}s^{-1}$ with the use of high-dielectric gate (HfO_2) due to enhanced screening of charged impurities [28]. To reduce extrinsic scattering, Cui et al. [48] developed a van der Waals (vdW) heterostructure device in which MoS_2 (single layer to six layers) is sandwiched between layers of BN as shown in Fig. 11(a), which enables a record-high mobility of 34000 $cm^2V^{-1}s^{-1}$ for six-layer MoS_2 at low temperature (Fig. 11(b)).

In addition, vdW heterostructure can also be used to constitute 2D tunneling FET (TFET) with two vertically stacked 2D layers as shown in Fig. 11(c) [115]. Compared to normal FET, TFET can reduce the voltage swing but maintain the same on/off ratio as show in Fig. 11(d) [2,116]. Therefore, TFETs are expected to break the 60mV-per-decade limit of subthreshold slope [38]. In TFET, the tunneling current can be boosted by suitable heterostructure with type-II or type-III band offsets [117]. This means that with suitable choice of the two 2D layers, such as one *n*-type and one *p*-type layer, it is possible to realize high tunneling current but low subthreshold slope. Recently, Wu et al. [118] reported the epitaxial growth of monolayer antimonene on a $PdTe_2$ substrate by molecular beam epitaxy for the first time. The antimonene is interacted by $PdTe_2$ via weak vdW force. This work opens a new way to fabricate vdW heterostructure for electronic and optoelectronic devices.

On the other hand, molecular modification can also be utilized to tune doping level through charge transfer for electronic devices. For example, Li et al. demonstrated *n*-type MoS_2 with benzyl viologen (BV) doping, *p*-type MoS_2 with $AuCl_3$ doping, and vertical MoS_2 *p*-*n* homogeneous junction as shown in Fig. 12(a) [119]. Current rectification and reversed current rectification are observed respectively in films thicker than 8 nm and thinner than 8 nm. Molecular doping is also a promising strategy to reduce contact resistance of 2D FETs since the contact resistance is another major factor limiting performance of FETs. The reduction of contact resistance can be achieved by degenerately doping of the contact region. Du et al. realized *n*-type doping of MoS_2 using polyethyleneimine (PEI, the

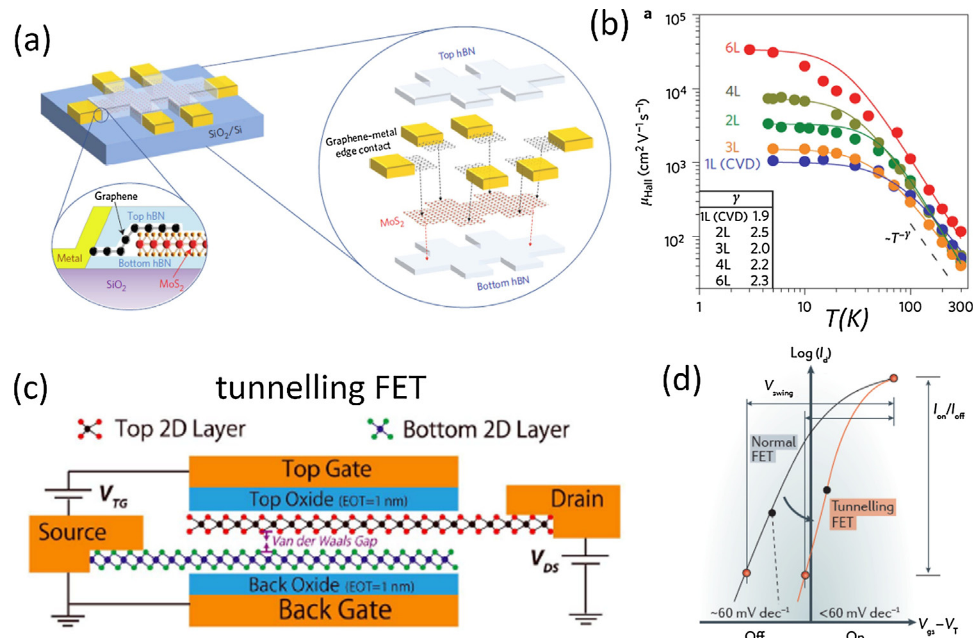

Fig. 11. Reducing impurity scattering and subthreshold value by vdW heterostructure. (a) Schematic diagram of the multi-layer device where MoS_2 is encapsulated by BN. (b) Hall mobility of the BN-encapsulated MoS_2 device as a function of temperature. (c) Schematic illustration of the tunneling FET, the structure of which consists of vertically stacked 2D layers. (d) Schematic diagram of transfer characteristics curve of a normal FET and a tunneling FET. (a) and (b), reprinted with permission from Ref. [48], Copyright 2015, Nature Publishing Group. (c), reprinted with permission from Ref. [115], Copyright 2015, IEEE. (d), reprinted with permission from Ref. [2], Copyright 2016, Nature Publishing Group.

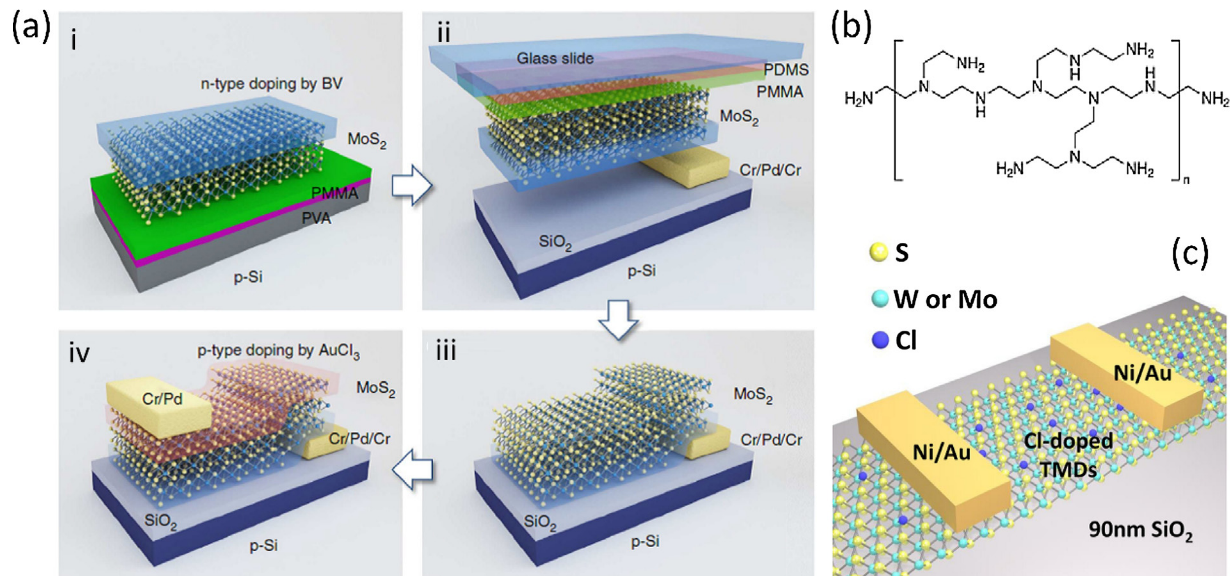

Fig. 12. Decreasing contact resistance by molecular doping. (a) Fabrication details of vertical *p-n* junction realized by $AuCl_3$ and benzyl viologen (BV) molecule doping. (a)-i, a MoS_2 flake was transferred on a PMMA/PVA/Si substrate (PMMA, polymethyl methacrylate; PVA, polyvinyl alcohol), and then BV-doped and annealed. (a)-ii, After dissolving the PVA layer in deionized water, the PMMA film supporting a MoS_2 flake was transferred to a PDMS/glass substrate(PDMS, polydimethylsiloxane). (a)-iii, The MoS_2 flake was stamped on the SiO_2/Si substrate, and the n-doped surface was aligned with the Cr/Pd/Cr bottom electrode prepared in advance. (a)-iv, After $AuCl_3$ doping and annealing, the vertical *p-n* junction in the MoS_2 flake was formed, followed by the deposition of a Cr/Pd top electrode. (b) Structure of polyethyleneimine (PEI) molecule, the n-type dopant of multilayer MoS_2. (c) Schematics of chloride-molecular-doped TMD FET. (a), reprinted with permission from Ref. [119], Copyright 2015, Nature Publishing Group. (b), reprinted with permission from Ref. [120], Copyright 2013, IEEE. (c), reprinted with permission from Ref. [121], Copyright 2014, American Chemical Society.

structure see Fig. 12(b)) as dopant source [120]. The resulting FET exhibits a 1.2 times reduction in contact resistance and 2.6 times in sheet resistance. In addition, Yang et al. adopted chloride molecular as *n*-type dopant for few-layer MoS_2 and WS_2, see Fig. 12(c) [121]. After doping, the contact resistance reduces significantly, to 0.5 kΩ μm and 0.7 kΩ μm for Ni-MoS_2 and No-WS_2 contacts respectively from (5–6) kΩ μm of undoped MoS_2 and 10^2 kΩ μm of undoped WS_2. The reduction of contact resistance via molecular doping is attributed to their excellent charge transfer from molecules. All these studies indicate that defect engineering is cru-

cial for the realization of 2D electronics and the improvement of device performance.

Conclusion and prospect

In summary, the semiconductor defect physics in emerging 2D semiconductors including their structural information probed by electron microscopy and optical characterization, and associated electronic properties evaluated by recent developed first-principles methods, together with their roles in engineering 2D electronic devices have been reviewed in this work. Particularly, ionization energy of defect by the analyses of WLZ extrapolation and Komsa correction are highlighted in 2D semiconductors. Also, we summarize the electronic device-related characteristics of defects in popular 2D semiconductors as a database, including carrier type, ionization energy, and carrier density. This review advances the systematic understanding of the defect's effects on electrical properties and electronic device performance. Although a lot of outstanding studies on 2D materials continue to emerge, the road to industrialization of 2D devices is likely to be long. Subsequent advancements in experiment and theory will be critical to achieve future 2D electronics. In experiment, controllable and stable doping process is the major device-related challenge for 2D semiconductors. In addition, some improved characterization techniques, which enable unraveling mysterious property are crucial. In theory and experiment, several specific topics for future research could be useful: i) Although defects in 2D semiconductors usually possess large ionization energies in theoretical prediction, they still contribute considerable conductivity in experiments, such as Re_{Mo} (natural *n*-type) and Nb_{Mo} (*p*-type) in MoS_2. This indicates that a unique defect ionization picture and carrier transport mechanism in 2D semiconductors could be existed and should be further explored. ii) Dynamic process monitoring of defect ionization and carrier transport by time-dependent density functional theory is also critical to understand electronic process for defects. iii) Ultrafast spectroscopy is used to study the defect property evolution with different dielectric environments. iv) Practicable *n*-type and *p*-type doping strategy for various device application should be selective for different 2D semiconductors; v) Exploration of doping limit rule in 2D semiconductors permits one to predict whether a 2D semiconductor can or cannot be doped to a certain type.

Acknowledgements

The work was supported by the National Natural Science Foundation of China (NSFC) and National Key Research and Development Program under Grants #61590930, #11374119, #2017YFB1104300, #2014CB921303, and #61435005. WQT thanks the support from the Open Projects of State Key Laboratory of Supramolecular Structure and Materials (JLU) (sklssm201723) and Key Laboratory of Polyoxometalate Science of Ministry of Education (NENU). D. Wang and X-. B. Li equally contribute to this work.

References

[1] G.R. Bhimanapati, Z. Lin, V. Meunier, Y. Jung, J. Cha, S. Das, et al., Acs Nano 9 (2015) 11509–11539.
[2] M. Chhowalla, D. Jena, H. Zhang, Nat. Rev. Mater. 1 (2016) 16052.
[3] M. Xu, T. Liang, M. Shi, H. Chen, Chem. Rev. 113 (2013) 3766–3798.
[4] J. Xiao, Z. Ye, Y. Wang, H. Zhu, Y. Wang, X. Zhang, Light: Sci. Appl. 4 (2015) e366.
[5] J. Yang, R. Xu, J. Pei, Y.W. Myint, F. Wang, Z. Wang, et al., Light: Sci. Appl. 4 (2015) e312.
[6] M. Zhao, Z. Ye, R. Suzuki, Y. Ye, H. Zhu, J. Xiao, et al., Light: Sci. Appl. 5 (2016) e16131.
[7] K.S. Novoselov, A.K. Geim, S.V. Morozov, D. Jiang, Y. Zhang, S.V. Dubonos, et al., Science 306 (2004) 666–669.
[8] F. Schwierz, Nat. Nanotechnol. 5 (2010) 487–496.
[9] K. Kim, J.-Y. Choi, T. Kim, S.-H. Cho, H.-J. Chung, Nature 479 (2011) 338–344.
[10] F. Xia, D.B. Farmer, Y.M. Lin, P. Avouris, Nano Lett. 10 (2010) 715–718.
[11] Y.-W. Son, M.L. Cohen, S.G. Louie, Phys. Rev. Lett. 97 (2006) 216803.
[12] E.V. Castro, K.S. Novoselov, S.V. Morozov, N.M. Peres, J.M. dos Santos, J. Nilsson, et al., Phys. Rev. Lett. 99 (2007) 216802.
[13] M.Y. Han, B. Özyilmaz, Y.B. Zhang, P. Kim, Phys. Rev. Lett. 98 (2007) 206805.
[14] D.W. Boukhvalov, M.I. Katsnelson, J. Phys.: Condens. Matter. 21 (2009) 344205.
[15] D.C. Elias, R.R. Nair, T.M.G. Mohiuddin, S.V. Morozov, P. Blake, M.P. Halsall, et al., Science 323 (2009) 610–613.
[16] G. Eda, C. Mattevi, H. Yamaguchi, H. Kim, M. Chhowalla, J. Phys. Chem. C 113 (2009) 15768–15771.
[17] D. Wang, D. Han, X.-B. Li, S.-Y. Xie, N.-K. Chen, W.Q. Tian, et al., Appl. Phys. Lett. 109 (2016) 203113.
[18] P. Vogt, P.D. Padova, C. Quaresima, J. Avila, E. Frantzeskakis, M.C. Asensio, et al., Phys. Rev. Lett. 108 (2012) 155501.
[19] M. Derivaz, D. Dentel, R. Stephan, M.C. Hanf, A. Mehdaoui, P. Sonnet, et al., Nano Lett. 15 (2015) 2510–2516.
[20] F.F. Zhu, W.J. Chen, Y. Xu, C.L. Gao, D.D. Guan, C.H. Liu, et al., Nat. Mater. 14 (2015) 1020–1025.
[21] Z. Shi, C.V. Singh, Nanoscale 9 (2017) 7055–7062.
[22] H. Liu, A.T. Neal, Z. Zhu, Z. Luo, X. Xu, D. Tomańek, et al., Acs Nano 8 (2014) 4033–4041.
[23] L. Li, Y. Yu, G.J. Ye, Q. Ge, X. Ou, H. Wu, et al., Nat. Nanotechnol. 9 (2014) 372–377.
[24] J. Qiao, X. Kong, Z.-X. Hu, F. Yang, W. Ji, Nat. Commun. 5 (2014) 4475.
[25] D.A. Bandurin, A.V. Tyurnina, G.L. Yu, A. Mishchenko, V. Zolyomi, S.V. Morozov, et al., Nat. Nanotechnol. 12 (2017) 223–227.
[26] P. Miro, M. Ghorbani-Asl, T. Heine, Angew. Chem. Int. Ed. Engl. 53 (2014) 3015–3018.
[27] S.B. Desai, S.R. Madhvapathy, A.B. Sachid, J.P. Llinas, Q. Wang, G.H. Ahn, et al., Science 354 (2016) 99–102.
[28] B. Radisavljevic, A. Radenovic, J. Brivio, V. Giacometti, A. Kis, Nat. Nanotechnol. 6 (2011) 147–150.
[29] M. Chhowalla, Z. Liu, H. Zhang, Chem. Soc. Rev. 44 (2015) 2584–2586.
[30] D. Pacile, J.C. Meyer, C.O. Girit, A. Zettl, Appl. Phys. Lett. 92 (2008) 133107.
[31] G.J. Slotman, A. Fasolino, J. Phys.: Condens. Matter. 25 (2013) 045009.
[32] A. Castellanos-Gomez, Nat. Photon. 10 (2016) 202–204.
[33] T. Cheiwchanchamnangij, W.R.L. Lambrecht, Phys. Rev. B 85 (2012) 205302.
[34] T.N. Theis, P.M. Solomon, Science 327 (2010) 1600.
[35] J.-P. Colinge, Solid State Electron. 48 (2004) 897–905.
[36] I. Ferain, C.A. Colinge, J.P. Colinge, Nature 479 (2011) 310–316.
[37] J. Kang, W. Cao, X. Xie, D. Sarkar, W. Liu, K. Banerjee, Proc. SPIE 9083 (2014) 908305.
[38] D. Jena, Proc. IEEE 101 (2013) 1585–1602.
[39] Y. Yoon, K. Ganapathi, S. Salahuddin, Nano Lett. 11 (2011) 3768–3773.
[40] L. Liu, Y. Lu, J. Guo, IEEE Trans. Electron Device 60 (2013) 4133.
[41] M. Tosun, S. Chuang, H. Fang, A.B. Sachid, M. Hettick, Y. Lin, et al., Acs Nano 8 (2014) 4948–4953.
[42] S. Wachter, D.K. Polyushkin, O. Bethge, T. Mueller, Nat. Commun. 8 (2017) 14948.
[43] F. Xia, H. Wang, D. Xiao, M. Dubey, A. Ramasubramaniam, Nat. Photon. 8 (2014) 899–907.
[44] K.F. Mak, J. Shan, Nat. Photon. 10 (2016) 216–226.
[45] A. Pospischil, M.M. Furchi, T. Mueller, Nat. Nanotechnol. 9 (2014) 257–261.
[46] C.H. Lee, G.H. Lee, A.M. van der Zande, W. Chen, Y. Li, M. Han, et al., Nat. Nanotechnol. 9 (2014) 676–681.
[47] H. Qiu, T. Xu, Z. Wang, W. Ren, H. Nan, Z. Ni, et al., Nat. Commun. 4 (2013) 2642.
[48] X. Cui, G.H. Lee, Y.D. Kim, G. Arefe, P.Y. Huang, C.H. Lee, et al., Nat. Nanotechnol. 10 (2015) 534–540.
[49] N.W. Ashcroft, N.D. Mermin, Solid State Phys. (1976).
[50] X. Zou, B.I. Yakobson, Acc. Chem. Res. 48 (2015) 73–80.
[51] W. Zhou, X. Zou, S. Najmaei, Z. Liu, Y. Shi, J. Kong, et al., Nano Lett. 13 (2013) 2615–2622.
[52] O.L. Krivanek, M.F. Chisholm, V. Nicolosi, T.J. Pennycook, G.J. Corbin, N. Dellby, et al., Nature 464 (2010) 571–574.
[53] C. Jin, F. Lin, K. Suenaga, S. Iijima, Phys. Rev. Lett. 102 (2009) 195505.
[54] N. Alem, O.V. Yazyev, C. Kisielowski, P. Denes, U. Dahmen, P. Hartel, et al., Phys. Rev. Lett. 106 (2011) 126102.
[55] H. Schmidt, F. Giustiniano, G. Eda, Chem. Soc. Rev. 44 (2015) 7715–7736.
[56] W. Zhao, R.M. Ribeiro, G. Eda, Acc. Chem. Res. 48 (2015) 91–99.
[57] J. Hong, Z. Hu, M. Probert, K. Li, D. Lv, X. Yang, et al., Nat. Commun. 6 (2015) 6293.
[58] H.-P. Komsa, J. Kotakoski, S. Kurasch, O. Lehtinen, U. Kaiser, A.V. Krasheninnikov, Phys. Rev. Lett. 109 (2012) 035503.
[59] Y.C. Lin, D.O. Dumcenco, H.P. Komsa, Y. Niimi, A.V. Krasheninnikov, Y.S. Huang, et al., Adv. Mater. 26 (2014) 2857–2861.
[60] J. Gao, Y.D. Kim, L. Liang, J.C. Idrobo, P. Chow, J. Tan, et al., Adv. Mater. 28 (2016) 9735–9743.
[61] S. Cho, S. Kim, J.H. Kim, J. Zhao, J. Seok, D.H. Keum, et al., Science 349 (2015) 625.
[62] Y. Wang, L. Li, W. Yao, S. Song, J.T. Sun, J. Pan, et al., Nano Lett. 15 (2015) 4013–4018.
[63] X. Lin, J.C. Lu, Y. Shao, Y.Y. Zhang, X. Wu, J.B. Pan, et al., Nat. Mat. 16 (2017) 717–721.

[64] Z. Wu, Z. Ni, Nanophotonics (2017).
[65] A. Eckmann, A. Felten, A. Mishchenko, L. Britnell, R. Krupke, K.S. Novoselov, et al., Nano Lett. 12 (2012) 3925–3930.
[66] W.M. Parkin, A. Balan, L. Liang, P.M. Das, M. Lamparski, C.H. Naylor, et al., Acs Nano 10 (2016) 4134–4142.
[67] A. Nipane, D. Karmakar, N. Kaushik, S. Karande, S. Lodha, Acs Nano 10 (2016) 2128–2137.
[68] S. Mignuzzi, A.J. Pollard, N. Bonini, B. Brennan, I.S. Gilmore, M.A. Pimenta, et al., Phys. Rev. B 91 (2015) 195411.
[69] E.D. Corro, H. Terrones, A. Elias, C. Fantini, S. Feng, M.A. Nguyen, et al., Acs Nano 8 (2014) 9629.
[70] Z. Wu, Z. Luo, Y. Shen, W. Zhao, W. Wang, H. Nan, et al., Nano Res. 9 (2016) 3622–3631.
[71] K.F. Mak, K. He, C. Lee, G.H. Lee, J. Hone, T.F. Heinz, et al., Nat. Mater. 12 (2013) 207–211.
[72] S. Mouri, Y. Miyauchi, K. Matsuda, Nano Lett. 13 (2013) 5944–5948.
[73] A.K.M. Newaz, D. Prasai, J.I. Ziegler, D. Caudel, S. Robinson, R.F. Haglund Jr., et al., Solid State Commun. 155 (2013) 49–52.
[74] S. Tongay, J. Zhou, C. Ataca, J. Liu, J.S. Kang, T.S. Matthews, et al., Nano Lett. 13 (2013) 2831–2836.
[75] H. Nan, Z. Wang, W. Wang, Z. Liang, Y. Lu, Q. Chen, et al., Acs Nano 8 (2014) 5738.
[76] S.B. Zhang, J. Phys. Condens. Matter 14 (2002) 881–903.
[77] J. Chocholoušová, V. Špirko, P. Hobza, Phys. Chem. Chem. Phys. 6 (2004) 37–41.
[78] C.G. Van de Walle, J. Appl. Phys. 95 (2004) 3851.
[79] A. Alkauskas, M.D. McCluskey, C.G. Van de Walle, J. Appl. Phys. 119 (2016) 181101.
[80] C. Freysoldt, B. Grabowski, T. Hickel, J. Neugebauer, G. Kresse, A. Janotti, et al., Rev. Mod. Phys. 86 (2014) 253–305.
[81] B. Huang, H. Lee, Phys. Rev. B 86 (2012) 245406.
[82] J.-Y. Noh, H. Kim, Y.-S. Kim, Phys. Rev. B 89 (2014) 205417.
[83] C.S. K, R.C. Longo, R. Addou, R.M. Wallace, K. Cho, Nanotechnology 25 (2014) 375703.
[84] K. Dolui, I. Rungger, C. Das Pemmaraju, S. Sanvito, Phys. Rev. B 88 (2013) 075420.
[85] Y. Liu, F. Xu, Z. Zhang, E.S. Penev, B.I. Yakobson, Nano Lett. 14 (2014) 6782–6786.
[86] S.B. Zhang, J.E. Northrup, Phys. Rev. Lett. 67 (1991) 2339–2342.
[87] D. Han, D. West, X.-B. Li, S.-Y. Xie, H.-B. Sun, S.B. Zhang, Phys. Rev. B 82 (2010) 155132.
[88] T. Yamabe, K. Yoshizawa, Y. Matsuura, K. Tanaka, Synth. Met. 75 (1995) 55–60.
[89] F. Bechstedt, A. Zywietz, J. Furthmuller, Europhys. Lett. 44 (1998) 309–314.
[90] S.B. Zhang, S.H. Wei, A. Zunger, Phys. Rev. B 63 (2001) 075205.
[91] C.H. Park, S.B. Zhang, S.-H. Wei, Phys. Rev. B 66 (2002) 073202.
[92] J.L. Lyons, A. Janotti, C.G. Van de Walle, Appl. Phys. Lett. 95 (2009) 252105.
[93] S.J. Pearton, F. Ren, A.P. Zhang, K.P. Lee, Mater. Sci. Eng. R 30 (2000) 55–212.
[94] J.L. Lyons, A. Janotti, C.G. Van de Walle, Phys. Rev. Lett. 108 (2012) 156403.
[95] S.G. Christenson, W. Xie, Y.Y. Sun, S.B. Zhang, J. Appl. Phys. 118 (2015) 135708.
[96] J.L. Lyons, A. Janotti, C.G. Van de Walle, Appl. Phys. Lett. 97 (2010) 152108.
[97] J. Lento, J.-L. Mozos, R.M. Nieminen, J. Phys. Condens. Matter 14 (2002) 2637–2645.
[98] D. Wang, D. Han, X.-B. Li, S.-Y. Xie, N.-K. Chen, W.Q. Tian, et al., Phys. Rev. Lett. 114 (2015) 196801.
[99] J. Ma, Z.G. Yu, Y.-W. Zhang, Phys. Rev. B 95 (2017) 165447.
[100] H.-P. Komsa, A. Pasquarello, Phys. Rev. Lett. 110 (2013) 095505.
[101] H.-P. Komsa, A.V. Krasheninnikov, Phys. Rev. B 91 (2015) 125304.
[102] J.-Y. Noh, H. Kim, M. Park, Y.-S. Kim, Phys. Rev. B 92 (2015) 115431.
[103] H.-P. Komsa, N. Berseneva, A.V. Krasheninnikov, R.M. Nieminen, Phys. Rev. X 4 (2014) 031044.
[104] D. Vinichenko, M.G. Sensoy, C.M. Friend, E. Kaxiras, arXiv (2017), 1701.02521v1.
[105] F. Li, Z. Hu, Z. Niu, L. Zhang, arXiv (2016), 1606.04185.
[106] S.-H. Wei, Comput. Mater. Sci. 30 (2004) 337–348.
[107] J. Suh, T.E. Park, D.Y. Lin, D. Fu, J. Park, H.J. Jung, et al., Nano Lett. 14 (2014) 6976–6982.
[108] E. Liu, Y. Fu, Y. Wang, Y. Feng, H. Liu, X. Wan, et al., Nat. Commun. 6 (2015) 6991.
[109] A. Prakash, Y. Cai, G. Zhang, Y.W. Zhang, K.W. Ang, Small 13 (2017) 1602909.
[110] K.S. Novoselov, D. Jiang, F. Schedin, T.J. Booth, V.V. Khotkevich, S.V. Morozov, et al., Proc. Natl. Acad. Sci. 102 (2005) 10451–10453.
[111] R. Kappera, D. Voiry, S.E. Yalcin, W. Jen, M. Acerce, S. Torrel, et al., APL Mater. 2 (2014) 092516.
[112] K. Kaasbjerg, K.S. Thygesen, K.W. Jacobsen, Phys. Rev. B 85 (2012) 115317.
[113] T. Gunst, T. Markussen, K. Stokbro, M. Brandbyge, Phys. Rev. B 93 (2016) 035414.
[114] Z. Yu, Y. Pan, Y. Shen, Z. Wang, Z.Y. Ong, T. Xu, et al., Nat. Commun. 5 (2014) 5290.
[115] M. Li, D. Esseni, J.J. Nahas, D. Jena, H.G. Xing, IEEE J. Electron Device Soc. 3 (2015) 200–207.
[116] Z. Qin, Z. Wei, A. Seabaugh, IEEE Electron Device Lett. 27 (2006) 297–300.
[117] G. Zhou, R. Li, M. Vasen, S. Chae, Y. Lu, et al., IEEE Int. Electron Devices Meet. (2012), 32.6.1–32.6.4.
[118] X. Wu, Y. Shao, H. Liu, Z. Feng, Y.L. Wang, J.T. Sun, et al., Adv. Mater. 29 (2017).
[119] H.M. Li, D. Lee, D. Qu, X. Liu, J. Ryu, A. Seabaugh, et al., Nat. Commun. 6 (2015) 6564.
[120] Y. Du, H. Liu, A.T. Neal, M. Si, P.D. Ye, IEEE Electron Device Lett. 34 (2013) 1328–1330.
[121] L. Yang, K. Majumdar, H. Liu, Y. Du, H. Wu, M. Hatzistergos, et al., Nano Lett. 14 (2014) 6275–6280.
[122] H. Li, Z. Yin, Q. He, H. Li, X. Huang, G. Lu, et al., Small 8 (2012) 63–67.
[123] H. Li, G. Lu, Z. Yin, Q. He, H. Li, Q. Zhang, et al., Small 8 (2012) 682–686.
[124] S. Kim, A. Konar, W.S. Hwang, J.H. Lee, J. Lee, J. Yang, et al., Nat. Commun. 3 (2012) 1011.
[125] B. Radisavljevic, M.B. Whitwick, A. Kis, Acs Nano 12 (2011) 9934–9938.
[126] M.R. Laskar, D.N. Nath, L. Ma, E.W. Lee II, C.H. Lee, T. Kent, et al., Appl. Phys. Lett. 104 (2014) 092104.
[127] M.W. Iqbal, M.Z. Iqbal, M.F. Khan, M.A. Shehzad, Y. Seo, J.H. Park, et al., Sci. Rep. 5 (2015) 10699.
[128] S.P. Koenig, R.A. Doganov, L. Seixas, A. Carvalho, J.Y. Tan, K. Watanabe, et al., Nano Lett. 16 (2016) 2145–2151.
[129] W. Feng, W. Zheng, W. Cao, P. Hu, Adv. Mater. 26 (2014) 6587–6593.
[130] S. Sucharitakul, N.J. Goble, U.R. Kumar, R. Sankar, Z.A. Bogorad, F.C. Chou, et al., Nano Lett. 15 (2015) 3815–3819.
[131] K.J. Saji, K. Tian, M. Snure, A. Tiwari, Adv. Electron. Mater. 2 (2016) 1500453.